

Chiral filtration and Faraday rotation in multi-Weyl semimetals

René Côté,¹ Rémi N. Duchesne,¹ Gautier D. Duchesne,¹ and Olivier Trépanier¹

¹*Département de physique and Institut Quantique,
Université de Sherbrooke, Sherbrooke, Québec, Canada J1K 2R1*

(Dated: April 4, 2023)

In Weyl semimetals with broken inversion and time-reversal symmetries, the Maxwell equations are modified by the presence of the axion terms \mathbf{b} and b_0 where, in the simplest case of a two-node Weyl semimetal, $2\hbar\mathbf{b}$ is the vector that connects two Weyl nodes in momentum space and $2\hbar b_0$ is the separation in energy of the two Dirac points of these nodes. These axion terms modify the behavior of electromagnetic waves inside a Weyl semimetal leading to a number of unique optical properties such as non-reciprocal propagation, circular and linear dichroism, birefringence and Faraday and Kerr rotations in the absence of a magnetic field. These effects can be used to design optical devices that act as broadband chiral filters, circular polarizers or tunable optical isolators. In this paper, we study in detail how the Faraday and Kerr rotations as well as the transmission and reflection of light incident on a slab of Weyl semimetal can be controlled by varying the different parameters characterizing the Weyl semimetal such as the axion terms, the Fermi level and Fermi velocity, the background dielectric constant, the scattering time for intraband scattering, the width of the semimetal and the dielectric constant of the dielectrics on each side of the semimetal slab. We extend our analysis to Weyl nodes with Chern number $n = 1, 2, 3$.

I. INTRODUCTION

According to the Nielsen-Ninomiya theorem¹, the simplest model of a Weyl semimetal with broken inversion and time-reversal symmetries consists of two Weyl nodes of opposite topological charge (or Chern number), $n = \pm 1$, separated in momentum space by $2\hbar\mathbf{b}$ and in energy by $2\hbar b_0$. Near these nodes, the electronic dispersion is linear in wave vector in all three directions of momentum space *i.e.* $E_s = s\hbar v_F |\mathbf{k}|$, where the wave vector \mathbf{k} is measured with respect to the Weyl point and $s = \pm 1$ is the band index (the upper and lower part of the Dirac cone). Density functional calculations suggest that more complex WSMs could host Weyl nodes with higher topological charge n . In these so-called multi-Weyl semimetals (mWSMs), the dispersion remains linear along the direction parallel to the vector \mathbf{b} but becomes quadratic (for $n = 2$) or cubic (for $n = 3$) in the perpendicular direction. The maximum topological charge, $n = 3$, is dictated by the discrete rotational symmetry on the lattice².

The topological nature of the band structure of WSMs leads to unusual transport properties such as an anomalous Hall effect³, a chiral-magnetic effect⁴, Fermi arcs on the surfaces parallel to the vector \mathbf{b} ⁵, a chiral anomaly leading to a negative longitudinal negative magnetoresistance⁶, a plasmon⁷ whose frequency increases as \sqrt{B} in a magnetic field B . These properties have been the subject of numerous reviews⁸.

Weyl semimetals also exhibit a number of surprising optical properties because the Maxwell equations that govern the propagation of electromagnetic waves in a WSM are modified by the inclusion of the axion terms \mathbf{b} and b_0 ^{9–11}. These terms generate an extra current $\mathbf{j} = -\frac{e^2}{2\pi^2\hbar}\mathbf{b} \times \mathbf{E} + \frac{e^2}{2\pi^2\hbar}b_0\mathbf{B}$ in the Ampère-Maxwell equation and an extra density $\rho = \frac{2\alpha}{\pi}\sqrt{\frac{\epsilon_0}{\mu_0}}\mathbf{b} \cdot \mathbf{B}$ in the Gauss law ($\alpha = e^2/4\pi\epsilon_0\hbar c$ is the fine-structure constant

and ϵ_0, μ_0 are the permittivity and permeability of free space). The modified Maxwell equations lead, in the absence of an external magnetic field, to giant optical nonreciprocity, circular and linear birefringence and dichroism and Faraday and Kerr rotations^{12,13}. Conversely, a study of the electromagnetic eigenmodes can give information about the band structure of a WSM such as the energy and momentum separations of the Weyl nodes and the position of the Fermi level¹⁴.

In the Faraday configuration where the light propagates in the direction of the axion term \mathbf{b} and in the absence of a magnetic field, the solutions of the Maxwell equations are forward and backward right-circularly (RCP) and left-circularly polarized (LCP) waves. When the propagation is perpendicular to \mathbf{b} (the Voigt configuration), the solutions are linearly polarized waves. It has previously been shown¹⁵ that a WSM can serve as a broadband chiral optical medium that selectively transmits and reflects circularly polarized electromagnetic wave in a wide range of frequencies when the wave vector \mathbf{q} of the electromagnetic wave is parallel to the axion term \mathbf{b} . When \mathbf{q} is perpendicular to \mathbf{b} , the WSM acts instead as a linear polarization filter, transmitting light when the polarization vector is collinear with \mathbf{b} and reflecting it otherwise. This chiral filtration effect has been considered in some recent papers where it was shown that the frequency range where the right or left circularly polarized light propagates can be controlled, to some extent, by changing the value of the axion term \mathbf{b} and/or the doping of the Weyl semimetal allowing the WSM to be used as a broadband polarizer and making the absorption perfectly tunable^{16–18}. These special optical properties of WSMs may be used in photonic applications and devices^{17,19,20}.

In this paper, we study in detail how the transmission, reflection and Kerr and Faraday rotations of an electromagnetic wave incident on a slab of a Weyl semimetal

are modified when the different parameters characterizing the WSM are varied. Our goal is to better understand the tunability of the chiral filtering and polarizing effects of WSMs. The list of parameters that we consider includes the polarization and frequency of the incident wave, the value of the axion terms \mathbf{b} and b_0 , the thickness d and Fermi level e_F (doping) of the WSM, the Fermi velocity v_F , the relaxation time τ for intraband transitions and the value of the background dielectric constant ε_b and cutoff wave vector k_c . We also consider the situation where the WSM is sandwiched between two dielectric media with different refractive indices n_1 and n_3 and extend our analysis to Weyl nodes with higher Chern numbers $n = 2, 3$. Since we work with a slab of WSM, we discuss the transmission resonances that occur when the wavelength of light in the WSM is comparable with the thickness d so that the WSM acts as a Fabry-Pérot interferometer. We extend our analysis to the thin-film limit $d \ll \lambda$, where λ is the wavelength of light in the WSM and to the limit $d \rightarrow \infty$ where the WSM is semi-infinite. Our study complements recent works on the subject^{18,21} by giving a more in-depth study of the effects of the different parameters characterizing the Weyl semimetal on some of its optical properties.

The remainder of this paper is organized as follows. In Sec. II, we define a simple model for the two-node WSM and compute the corresponding dielectric tensor. Section III is devoted to the derivation of the dispersion relation and polarization of the propagating waves inside the WSM when the propagation is along the vector connecting both nodes. In Sec. IV, we apply the Maxwell boundary conditions to derive the transmission and reflection coefficients for the RCP, LCP and linearly polarized (LP) waves and the Faraday and Kerr rotation and ellipticity angles of the transmitted and reflected waves. Our numerical results are presented and discussed in Sec. V. We conclude in Sec. VI.

II. HAMILTONIAN OF A MULTI-WEYL SEMIMETAL

We consider a two-node model of a Weyl semimetal with broken inversion and time-reversal symmetries so that the two nodes of opposite chiralities are separated in momentum space and in energy. The nodes are centered at wave vectors $\chi b \hat{\mathbf{z}}$ in the Brillouin zone and separated in energy by $2\hbar b_0$, where $\chi = \pm 1$ stands for the node index. We assume that the two nodes are untilted and that there is no external magnetic field. In the continuum approximation, which is valid for small wave vector deviations from a Weyl node, the Hamiltonian of an electron in node χ with Chern number $C = n$, with $n = 1, 2, 3$, is given by²

$$h_\chi(\mathbf{k}) = \chi \hbar v_F [k_z \sigma_z + \beta (k_-^n \sigma_+ + k_+^n \sigma_-)] + \chi \hbar b_0 I_2, \quad (1)$$

where v_F is the Fermi velocity for the dispersion in k_z , β characterizes the anisotropy in the dispersion (β has

units m^{n-1}), \mathbf{k} is the wave vector measured from the position of the Weyl node, σ is the vector of Pauli matrices defined in the basis of the two electronic bands that cross and I_2 is the 2×2 unit matrix. We have also defined $\sigma_\pm = \sigma_x \pm i\sigma_y$ and $k_\pm = k_x \pm ik_y$. The terms \mathbf{b} and b_0 break time-reversal and space-inversion symmetry respectively. According to Ref. 2: "C₄ or C₆ symmetry in a crystal can protect double-Weyl nodes while only C₆ symmetry can protect triple-Weyl nodes. There cannot be any higher order crossings protected by n -fold rotation symmetries".

The electronic energy spectrum for each node is given in cylindrical coordinates by

$$E_s(\mathbf{k}) = s \hbar v_F \sqrt{k_z^2 + \beta^2 k_\perp^{2n}} + \chi \hbar b_0, \quad (2)$$

where $s = \pm 1$ is the band index. The corresponding eigenstates are given by

$$|\eta_{s,\chi}(\mathbf{k})\rangle = \frac{1}{h_{s,\chi}} \begin{pmatrix} k_z + \chi s \sqrt{k_z^2 + \beta^2 k_\perp^{2n}} \\ \beta k_\perp^n e^{in\varphi} \end{pmatrix}, \quad (3)$$

where $h_{s,\chi}$ is a normalization constant. We assume that the two nodes are at a thermodynamical equilibrium at $T = 0$ K and share a common Fermi level e_F so that the local Fermi level energy $e_{F,\chi}$ in each node is given by

$$e_{F,\tau} = e_F - \chi \hbar b_0. \quad (4)$$

For Chern number $n = 1$, the Hamiltonian is isotropic in \mathbf{k} around each Weyl node so that the (relative) dielectric tensor is isotropic, $\varepsilon_{ij}(\omega) = \varepsilon(\omega) \delta_{ij}$. This is no longer true if $n \neq 1$ and we have instead²² that $\varepsilon_{xx} = \varepsilon_{yy} = \varepsilon(\omega)$ with $\varepsilon(\omega)$ given by

$$\begin{aligned} \varepsilon(\omega) = \varepsilon_b & \quad (5) \\ & + \gamma \sum_\chi \left[i\theta \left(\omega - \frac{2e_{F,\chi}}{\hbar} \right) + \frac{1}{\pi} \ln \left(\left| \frac{\omega^2 - 4v_F^2 k_c^2}{\omega^2 - 4e_{F,\chi}^2 / \hbar^2} \right| \right) \right] \\ & + \gamma \sum_\chi \frac{4}{\pi \hbar^2 \omega} \frac{i\tau}{1 + \omega^2 \tau^2} \left(e_{F,\chi}^2 + \frac{1}{3} \hbar^2 \omega^2 + \frac{\hbar^2}{4\tau^2} \right) \\ & - \gamma \sum_\chi \frac{4}{\pi \hbar^2} \frac{\tau^2}{1 + \omega^2 \tau^2} \left(e_{F,\chi}^2 - \frac{\hbar^2}{12\tau^2} \right), \end{aligned}$$

where we have defined

$$\gamma = \frac{n\alpha}{6v_F/c} \quad (6)$$

and $\alpha = e^2/4\pi\varepsilon_0\hbar c$ is the fine-structure constant with ε_0, μ_0 the permittivity and permeability of free space, k_c is a higher-energy cutoff wave vector, and ε_b is the (relative) background dielectric constant that can be large in WSMs. For example $\varepsilon_b = 6.2$ in WSM TaAs²³. The dependence of $\varepsilon_{zz}(\omega)$ on the Chern number n is more complex²¹ and we do not give it here since it is not needed in any of the calculations in this paper.

The first (last) two lines in Eq. (5) are contributions from the interband (intra-band) transitions with τ the relaxation time for the intra-band transitions. Both contributions, for Chern number $n = 1$, have been calculated in parts in a number of papers^{12,13,24-28}. It is easy to show²² that the only difference for Chern number n is a multiplication of the conductivities σ_{xx} and σ_{yy} , calculated with $n = 1$, by the Chern number n . For completeness, we give a proof of this statement in Appendix A. The off-diagonal conductivity $\sigma_{xy}(\omega)$ scales with n in the same way. To order ω^2 , it is given by^{18,22}

$$\text{Re}[\sigma_{xy}(\omega)] = \frac{ne^2b}{\pi\hbar} \left(1 + \frac{1}{12} \frac{\omega^2}{v_F^2 k_c^2 - v_F^2 b^2} \right). \quad (7)$$

With the parameters that we use in this paper, the ω^2 correction is negligible and we ignore it in our calculations.

The density of states measured with respect to the Dirac point in each node is defined by $g(E) = \frac{1}{V} \sum_{\mathbf{k}} \delta(E - E(\mathbf{k}))$. With $E(\mathbf{k}) = \hbar v_F \sqrt{k_z^2 + \beta^2 k_{\perp}^2}$, it is given for $n = 1, 2, 3$ by $g_n(E)$ where

$$g_1(E) = \frac{E^2}{2\pi^2 \beta^2 \hbar^3 v_F^3}, \quad (8)$$

$$g_2(E) = \frac{E}{8\pi \beta \hbar^2 v_F^2}, \quad (9)$$

$$g_3(E) = \frac{E^{2/3}}{12\beta^{2/3} \pi^{3/2} (\hbar v_F)^{5/3}} \frac{\Gamma(\frac{1}{3})}{\Gamma(\frac{5}{6})}. \quad (10)$$

The total electronic density $n_{e,n}$ in the WSM is thus related to the Fermi level e_F by

$$n_{e,1} = e_F \frac{3\hbar^2 b_0^2 + e_F^2}{3\pi^2 \beta^2 \hbar^3 v_F^3}, \quad (11)$$

$$n_{e,2} = \frac{\hbar^2 b_0^2 + e_F^2}{8\pi \beta \hbar^2 v_F^2}, \quad (12)$$

$$n_{e,3} = \frac{\left((e_F + \hbar b_0)^{5/3} + (e_F - \hbar b_0)^{5/3} \right) \Gamma(\frac{1}{3})}{20\beta^{2/3} \pi^{3/2} (\hbar v_F)^{5/3} \Gamma(\frac{5}{6})}. \quad (13)$$

III. ELECTROMAGNETIC MODES

The Maxwell equations in a WSM with Chern number $n = 1$ are modified by the presence of the axion field $\theta(\mathbf{r}, t) = 2\mathbf{b} \cdot \mathbf{r} - 2b_0 t$ and become¹¹

$$\nabla \cdot \mathbf{D} = \rho_f + \frac{2\alpha}{\pi} \sqrt{\frac{\varepsilon_0}{\mu_0}} \mathbf{b} \cdot \mathbf{B}, \quad (14)$$

$$\nabla \cdot \mathbf{B} = 0, \quad (15)$$

$$\nabla \times \mathbf{E} = -\frac{\partial \mathbf{B}}{\partial t}, \quad (16)$$

$$\nabla \times \mathbf{H} = \frac{\partial \mathbf{D}}{\partial t} + \mathbf{J}_f - \frac{2\alpha}{\pi} \sqrt{\frac{\varepsilon_0}{\mu_0}} (\mathbf{b} \times \mathbf{E} - b_0 \mathbf{B}). \quad (17)$$

In these equations, ρ_f is the free (or induced) charge density and $\mathbf{J}_f = \sigma(\omega) \mathbf{E}$ is the induced current density with

the conductivity obtained from $\varepsilon(\omega) = \varepsilon_b + i\sigma(\omega)/\varepsilon_0\omega$ with $\varepsilon(\omega)$ given in Eq. (5). We assume that the relative permeability $\mu_r = \mu/\mu_0$ is unity. In mWSMs, Eq. (7) shows that \mathbf{b} is replaced by $n\mathbf{b}$ in the Maxwell equations. This also true for b_0 which is replaced by nb_0 ²⁹. The gyrotropic effect of b_0 is very small in comparison with that due to \mathbf{b} so that we neglect its presence in the Maxwell equations¹³. We keep b_0 in the calculation of $\sigma(\omega)$, however, since it determines the density of electrons in each node.

The wave equation can be written as $M_{i,j} E_j = 0$ where the matrix M is defined by

$$M_{ij}(\omega) = -c^2 (q^2 \delta_{ij} - q_i q_j) + \omega^2 \tilde{\varepsilon}_{ij}, \quad (18)$$

where δ_{ij} is the Kronecker delta and the effective dielectric tensor $\tilde{\varepsilon}_{ij}$ is given by

$$\tilde{\varepsilon}_{ij}(\omega) = \varepsilon(\omega) \delta_{ij} + \frac{2in\alpha c}{\pi\omega} \varepsilon_{ijk} b_k, \quad (19)$$

where ε_{ijk} is the Levi-Civita symbol. The axion term \mathbf{b} thus appears as an off-diagonal term in the effective dielectric tensor of a WSM.

In this paper, we work in the so-called Faraday configuration: we take $\mathbf{b} = b\hat{\mathbf{z}}$ and consider a wave propagating along the z axis so that we have, for the matrix M , the simple form

$$M = \begin{pmatrix} \omega^2 \varepsilon(\omega) - c^2 q^2 & in\omega\kappa cb & 0 \\ -in\omega\kappa cb & \omega^2 \varepsilon(\omega) - c^2 q^2 & 0 \\ 0 & 0 & \omega^2 \varepsilon_{zz}(\omega) \end{pmatrix}, \quad (20)$$

with the newly defined constant $\kappa = 2\alpha/\pi$. The dispersion relations of the electromagnetic modes are given by

$$q_{1,\pm} = \pm \frac{\omega}{c} \sqrt{\varepsilon_+(\omega)}, \quad (21)$$

$$q_{2,\pm} = \pm \frac{\omega}{c} \sqrt{\varepsilon_-(\omega)}, \quad (22)$$

where the dielectric functions

$$\varepsilon_{\pm}(\omega) = \varepsilon(\omega) \pm \frac{n\kappa b}{\omega} \quad (23)$$

give the complex refractive indices

$$n_{\pm}(\omega) = \sqrt{\varepsilon_{\pm}(\omega)}. \quad (24)$$

The polarization vectors \mathbf{e}_+ for the modes $q_{1,\pm}$ and \mathbf{e}_- for the modes $q_{2,\pm}$ are given by

$$\mathbf{e}_+ = \frac{1}{\sqrt{2}} \begin{pmatrix} i \\ 1 \\ 0 \end{pmatrix}; \quad \mathbf{e}_- = \frac{1}{\sqrt{2}} \begin{pmatrix} -i \\ 1 \\ 0 \end{pmatrix}. \quad (25)$$

The wave vectors $q_{1,+}$ ($q_{1,-}$) correspond to the forward (backward) propagation of a right (left)-circularly polarized (RCP and LCP) wave while $q_{2,+}$ ($q_{2,-}$) correspond to the forward (backward) propagation of a left

(right)-circularly polarized wave. For a given circular polarization, the dielectric function is different for forward and backward propagations *i.e.* the axion term leads to non-reciprocal propagation of the electromagnetic waves. Moreover, the dielectric function is different for RCP and LCP wave so that the WSM exhibits circular birefringence as well as circular dichroism since the two waves are attenuated differently. Dispersion relations for other direction of propagation have also been derived¹⁴.

IV. TRANSMISSION AND REFLECTION COEFFICIENTS

In order to calculate the transmission and reflection coefficients, we consider a monochromatic electromagnetic wave with amplitude E_0 impinging at normal incidence on the surface of a WSM that we take at $z = 0$ and propagating along the direction of the axion vector $\mathbf{b} = b\hat{\mathbf{z}}$. This Faraday configuration is the simplest to study since there is no Fermi arc on the surfaces perpendicular to the vector \mathbf{b} . The slab of WSM occupies region 2 defined by $z \in [0, d]$, where d is the width of the WSM. Medium 1 ($z < 0$) and 3 ($z > d$) are dielectrics with refractive indices n_1 and n_3 respectively. The electric and magnetic fields in regions 1 and 3 are given by

$$\begin{aligned} \mathbf{E}_1(z, t) &= E_0 \left[\mathbf{e}_i e^{i(q_i z - \omega t)} + r \mathbf{e}_r e^{-i(q_i z + \omega t)} \right], \\ \mathbf{B}_1(z, t) &= \frac{q_i}{\omega} E_0 \left[(\hat{\mathbf{z}} \times \mathbf{e}_i) e^{i(q_i z - \omega t)} - r (\hat{\mathbf{z}} \times \mathbf{e}_r) e^{-i(q_i z + \omega t)} \right], \end{aligned} \quad (26)$$

and

$$\begin{aligned} \mathbf{E}_3(z, t) &= E_0 t \mathbf{e}_t e^{i(q_t z - \omega t)}, \\ \mathbf{B}_3(z, t) &= \frac{q_t}{\omega} E_0 t (\hat{\mathbf{z}} \times \mathbf{e}_t) e^{i(q_t z - \omega t)}, \end{aligned} \quad (27)$$

where r and t are reflection and transmission factors and the \mathbf{e}' s are polarization vectors. The incident and transmitted wave vectors are given by

$$q_i = q_0 n_1, \quad (28)$$

$$q_t = q_0 n_3, \quad (29)$$

where $q_0 = \omega/c$. We write the polarization vectors as

$$\mathbf{e}_i = \alpha_i \hat{\mathbf{x}} + \beta_i \hat{\mathbf{y}}, \quad (30)$$

$$\mathbf{e}_t = \alpha_t \hat{\mathbf{x}} + \beta_t \hat{\mathbf{y}}. \quad (31)$$

Inside the WSM, there are four propagating waves so

that the electric and magnetic fields are given by

$$\mathbf{E}_2(z, t) = \sum_{n=1}^{n=4} E_0 t_n \mathbf{e}_n e^{i(q_n z - \omega t)}, \quad (32)$$

$$\mathbf{B}_2(z, t) = \sum_{n=1}^{n=4} \frac{q_n}{\omega} E_0 t_n (\hat{\mathbf{z}} \times \mathbf{e}_n) e^{i(q_n z - \omega t)}, \quad (33)$$

with the polarization vectors written as

$$\mathbf{e}_n = \alpha_n \hat{\mathbf{x}} + \beta_n \hat{\mathbf{y}}. \quad (34)$$

t_1	$q_1 = q_{1+}, \mathbf{e}_1 = \mathbf{e}_+$	F-RCP
t_2	$q_2 = q_{1-}, \mathbf{e}_2 = \mathbf{e}_+$	B-LCP
t_3	$q_3 = q_{2+}, \mathbf{e}_3 = \mathbf{e}_-$	F-LCP
t_4	$q_4 = q_{2-}, \mathbf{e}_4 = \mathbf{e}_-$	B-RCP

TABLE I. Description of the coefficients t_n .

The factors t_n correspond to forward (F) and backward (B) propagations along the z axis with RCP and LCP polarization as described in Table 1.

At each surface of the WSM ($z = 0$ and $z = d$), the electric and magnetic field must satisfy the Maxwell boundary conditions

$$(\mathbf{D}_i - \mathbf{D}_f) \cdot \hat{\mathbf{n}} = 0, \quad (35)$$

$$\mathbf{E}_{i,\parallel} - \mathbf{E}_{f,\parallel} = 0, \quad (36)$$

$$(\mathbf{B}_i - \mathbf{B}_f) \cdot \hat{\mathbf{n}} = 0, \quad (37)$$

$$\mathbf{B}_{i,\parallel} - \mathbf{B}_{f,\parallel} = 0, \quad (38)$$

where the unit vector $\hat{\mathbf{n}}$ points from medium f to medium i . In the two dielectric media, $\mathbf{D}_1 = n_1^2 \mathbf{E}_1$ and $\mathbf{D}_3 = n_3^2 \mathbf{E}_3$ while in the WSM $D_i = \tilde{\epsilon}_{ij} E_j$. The boundary conditions lead to the system of equations

$$\alpha_i + r \alpha_r = \sum_{n=1}^{n=4} t_n \alpha_n; \quad \alpha_i - r \alpha_r = \sum_{n=1}^{n=4} \frac{q_n}{q_i} t_n \alpha_n, \quad (39)$$

$$\beta_i + r \beta_r = \sum_{n=1}^{n=4} t_n \beta_n; \quad \beta_i - r \beta_r = \sum_{n=1}^{n=4} \frac{q_n}{q_i} t_n \beta_n, \quad (40)$$

$$t \alpha_t e^{iq_t d} = \sum_{n=1}^{n=4} t_n \alpha_n e^{iq_n d} = \sum_{n=1}^{n=4} \frac{q_n}{q_t} t_n \alpha_n e^{iq_n d}, \quad (41)$$

$$t \beta_t e^{iq_t d} = \sum_{n=1}^{n=4} t_n \beta_n e^{iq_n d} = \sum_{n=1}^{n=4} \frac{q_n}{q_t} t_n \beta_n e^{iq_n d}. \quad (42)$$

In matrix form, and using Eqs. (21)-(22) and Eq. (25), the system of equations is given by

$$\frac{1}{\sqrt{2}} \begin{pmatrix} \sqrt{2} & 0 & -i & -i & i & i & 0 & 0 \\ 0 & \sqrt{2} & -1 & -1 & -1 & -1 & 0 & 0 \\ 0 & \sqrt{2} & \frac{n_+}{n_1} & -\frac{n_+}{n_1} & \frac{n_-}{n_1} & -\frac{n_-}{n_1} & 0 & 0 \\ -\sqrt{2} & 0 & -\frac{in_+}{n_1} & \frac{in_+}{n_1} & \frac{in_-}{n_1} & -\frac{in_-}{n_1} & 0 & 0 \\ 0 & 0 & ie^{in_+\xi} & ie^{-in_+\xi} & -ie^{in_-\xi} & -ie^{-in_-\xi} & -\sqrt{2}e^{in_3\xi} & 0 \\ 0 & 0 & e^{in_+\xi} & e^{-in_+\xi} & e^{in_-\xi} & e^{-in_-\xi} & 0 & -\sqrt{2}e^{in_3\xi} \\ 0 & 0 & \frac{n_+e^{in_+\xi}}{n_3} & -\frac{n_+e^{-in_+\xi}}{n_3} & \frac{n_-e^{in_-\xi}}{n_3} & -\frac{n_-e^{-in_-\xi}}{n_3} & 0 & -\sqrt{2}e^{in_3\xi} \\ 0 & 0 & \frac{in_+e^{in_+\xi}}{n_3} & -\frac{in_+e^{-in_+\xi}}{n_3} & -\frac{in_-e^{in_-\xi}}{n_3} & \frac{in_-e^{-in_-\xi}}{n_3} & -\sqrt{2}e^{in_3\xi} & 0 \end{pmatrix} \begin{pmatrix} r\alpha_r \\ r\beta_r \\ t_1 \\ t_2 \\ t_3 \\ t_4 \\ t\alpha_t \\ t\beta_t \end{pmatrix} = \begin{pmatrix} -\alpha_i \\ -\beta_i \\ \beta_i \\ -\alpha_i \\ 0 \\ 0 \\ 0 \\ 0 \end{pmatrix}, \quad (43)$$

where we have defined the parameter

$$\xi = q_0 d = \frac{\omega d}{c}. \quad (44)$$

Inverting the matrix in Eq. (43) gives the eight unknown factors in terms of the polarization of the incident wave and the optical properties of the three media. We remark that our procedure is not the standard way of obtaining these factors¹⁶. It would become cumbersome with many interfaces. But, with only two interfaces, the 8×8 matrix is easily invertible by Mathematica or any other symbolic software.

The time-averaged energy current is given by the Poynting vector $\langle \mathbf{S} \rangle = \frac{1}{2\mu_0} \text{Re} [\mathbf{E} \times \mathbf{B}^*]$ so that we have in medium 1 and 3

$$\langle \mathbf{S}_1 \rangle \cdot \hat{\mathbf{z}} = \frac{1}{2\mu_0} \frac{n_1}{c} E_0^2, \quad (45)$$

$$\langle \mathbf{S}_3 \rangle \cdot \hat{\mathbf{z}} = \frac{1}{2\mu_0} E_0^2 \frac{n_3}{c} (|t\alpha_t|^2 + |t\beta_t|^2). \quad (46)$$

The transmission and reflection coefficients are defined by

$$T = \frac{\langle \mathbf{S}_3 \rangle_{\text{transmitted}} \cdot \hat{\mathbf{z}}}{\langle \mathbf{S}_1 \rangle_{\text{incident}} \cdot \hat{\mathbf{z}}} = \frac{n_3}{n_1} (|t\alpha_t|^2 + |t\beta_t|^2), \quad (47)$$

and

$$R = \frac{\langle \mathbf{S}_1 \rangle_{\text{reflected}} \cdot \hat{\mathbf{z}}}{\langle \mathbf{S}_1 \rangle_{\text{incident}} \cdot \hat{\mathbf{z}}} = |r\alpha_t|^2 + |r\beta_t|^2 \quad (48)$$

respectively.

A. RCP wave

For an incident RCP wave, the polarization vector is $\mathbf{e}_i = \mathbf{e}_+ = \frac{1}{\sqrt{2}}(i, 1, 0)$ so that $\alpha_i = 1$ and $\beta_i = 1$. The polarization vector turns clockwise when looking in the direction of propagation of the wave. (It satisfies the right-hand rule with the thumb pointing in the direction of the axion vector \mathbf{b} and the fingers in the direction of rotation of the polarization vector¹⁵.) Solving the system of equations, we get the factors

$$t\alpha_t = -\sqrt{2}A_+, \quad (49)$$

$$t\beta_t = \sqrt{2}iA_+, \quad (50)$$

where we have defined

$$A_+ = \frac{n_1 n_+ e^{-in_3 \xi}}{(n_1 n_3 + n_+^2) \sin(n_+ \xi) + i(n_1 + n_3) n_+ \cos(n_+ \xi)}. \quad (51)$$

Moreover, inside the WSM, we have for the factors t_n

$$t_1 = \frac{in_1(n_+ + n_3)e^{-in_+\xi}}{(n_1 n_3 + n_+^2) \sin(n_+ \xi) + n_+ i(n_1 + n_3) \cos(n_+ \xi)} \quad (52)$$

$$t_2 = \frac{in_1(n_+ - n_3)e^{in_+\xi}}{(n_1 n_3 + n_+^2) \sin(n_+ \xi) + n_+ i(n_1 + n_3) \cos(n_+ \xi)} \quad (53)$$

$$t_3 = 0, \quad (54)$$

$$t_4 = 0. \quad (55)$$

The transmitted wave is also an RCP wave and only the F-RCP which is reflected as B-LCP are present in the WSM.

The reflection factors are given by

$$r\alpha_r = \frac{i}{\sqrt{2}}C_+, \quad (56)$$

$$r\beta_r = \frac{1}{\sqrt{2}}C_+, \quad (57)$$

where we have defined

$$C_+ = \frac{(n_1 n_3 - n_+^2) \sin n_+ \xi + n_+ i(n_1 - n_3) \cos n_+ \xi}{(n_1 n_3 + n_+^2) \sin n_+ \xi + n_+ i(n_1 + n_3) \cos n_+ \xi}. \quad (58)$$

Upon reflection at the interface between regions 1 and 2, the RCP wave becomes a LCP wave since the polarization vector does not change but the direction of propagation is reversed.

The transmission and reflection coefficients for the RCP wave are given by

$$T_+ = T_{RCP} = 4 \frac{n_3}{n_1} |A_+|^2, \quad (59)$$

$$R_+ = R_{RCP} = |C_+|^2. \quad (60)$$

B. LCP wave

For an incident LCP wave, the polarization vector is $\mathbf{e}_i = \mathbf{e}_- = \frac{1}{\sqrt{2}}(-i, 1, 0)$ so that $\alpha_i = -i$ and $\beta_i = 1$.

Solving the system of equations, we get

$$t\alpha_t = \sqrt{2}A_-, \quad (61)$$

$$t\beta_t = \sqrt{2}iA_-, \quad (62)$$

where we have defined

$$A_- = \frac{n_1 n_- e^{-in_3 \xi}}{(n_1 n_3 + n_-^2) \sin(n_- \xi) + i(n_1 + n_3) n_- \cos(n_- \xi)}. \quad (63)$$

Inside the WSM, the factors t_n are given by

$$t_1 = 0, \quad (64)$$

$$t_2 = 0, \quad (65)$$

$$t_3 = \frac{in_1(n_- + n_3)e^{-in_- \xi}}{(n_1 n_3 + n_-^2) \sin(n_- \xi) + n_- i(n_1 + n_3) \cos(n_- \xi)} \quad (66)$$

$$t_4 = \frac{in_1(n_- - n_3)e^{in_- \xi}}{(n_1 n_3 + n_-^2) \sin(n_- \xi) + n_- i(n_1 + n_3) \cos(n_- \xi)} \quad (67)$$

The transmitted wave is also a LCP wave. Only the F-LCP and the reflected B-RCP waves are present in the WSM.

For the reflection factors, we have

$$r\alpha_r = \frac{-i}{\sqrt{2}}C_-, \quad (68)$$

$$r\beta_r = \frac{1}{\sqrt{2}}C_-, \quad (69)$$

where we have defined

$$C_- = \frac{(n_1 n_3 - n_-^2) \sin n_- \xi + n_- i(n_1 - n_3) \cos n_- \xi}{(n_1 n_3 + n_-^2) \sin n_- \xi + n_- i(n_1 + n_3) \cos n_- \xi}. \quad (70)$$

The transmission and reflection coefficients for the LCP wave are then

$$T_- = T_{LCP} = 4 \frac{n_3}{n_1} |A_-|^2, \quad (71)$$

$$R_- = R_{LCP} = |C_-|^2. \quad (72)$$

C. LP wave

An incident linear polarization vector can be decomposed on the RCP-LCP basis. For $\mathbf{e}_i = \hat{\mathbf{x}}$, we have $\alpha_i = 1$ and $\beta_i = 0$ and $\mathbf{e}_i = \frac{-i}{\sqrt{2}}(\mathbf{e}_+ - \mathbf{e}_-)$. The transmission factors are given by

$$t\alpha_t = i(A_+ + A_-), \quad (73)$$

$$t\beta_t = A_+ - A_-, \quad (74)$$

while we have for the reflection factors

$$r\alpha_r = \frac{1}{2}(C_+ + C_-), \quad (75)$$

$$r\beta_r = \frac{i}{2}(C_- - C_+). \quad (76)$$

The four factors t_n are nonzero in this case and given by $\frac{-i}{\sqrt{2}}t_1$, $\frac{-i}{\sqrt{2}}t_2$, $\frac{i}{\sqrt{2}}t_3$, and $\frac{i}{\sqrt{2}}t_4$.

Because of the rotational symmetry of the WSM around the axis of propagation (the axion term \mathbf{b} being along this axis), we get for any orientation of \mathbf{e}_i in the xy -plane that the transmission and reflection coefficients are given by

$$T_{LP} = 2 \frac{n_3}{n_1} (|A_+|^2 + |A_-|^2) \quad (77)$$

and

$$R_{LP} = \frac{1}{2} (|C_+|^2 + |C_-|^2). \quad (78)$$

D. Transmission resonances

Depending on the thickness of the WSM and the frequency of the incident electromagnetic wave, an oscillatory pattern in the transmission coefficients $T_{\pm}(\omega)$ can occur. Transmission resonances in the frequency range where an RCP wave propagates with almost no dissipation (*i.e.* n_+ is real and positive in the clean limit) occur when $\cos^2(n_+ \xi) = 1$ or $\sin^2(n_+ \xi) = 1$. In the first case, we have at resonance

$$T_{+,1} = 4 \frac{n_1 n_3}{(n_1 + n_3)^2}, \quad (79)$$

while in the second case

$$T_{+,2} = 4 \frac{n_1 n_3 n_+^2}{(n_1 n_3 + n_+^2)^2}. \quad (80)$$

The maxima are given by the condition $\sin^2(n_+ \xi) = 1$ if n_+ is between n_1 and n_3 in value since then $T_{+,2} > T_{+,1}$. They are given by $\cos^2(n_+ \xi) = 1$ otherwise. When $\cos^2(n_+ \xi) = 1$, we have inside the WSM, for the two waves

$$t_2 = t_1 \frac{(n_+ - n_3)}{(n_+ + n_3)}, \quad (81)$$

while, when $\sin^2(n_+ \xi) = 1$, there is a phase shift of π *i.e.*

$$t_2 = -t_1 \frac{(n_+ - n_3)}{(n_+ + n_3)}. \quad (82)$$

At precisely $n_1 = n_+$ or $n_3 = n_+$, we have $T_{+,1} = T_{+,2}$ and the oscillatory pattern in the transmission T_+ disappears. The same remark applies to T_- with n_+ replaced by n_- . When $n_1 = n_3$ (case 2 above), $T_{\pm} = 1$ and $R_{\pm} = 0$. There is no oscillation and no reflection in this case and the transmission is maximal.

The requirement that $\cos^2(n_{\pm} \xi) = 1$ is equivalent to the quantization condition

$$d = m \frac{\lambda_{\pm}}{2}, \quad (83)$$

and for $\sin^2(n_{\pm}\xi) = 1$ to

$$d = (2m + 1) \frac{\lambda_{\pm}}{4}, \quad (84)$$

where $m = 1, 2, 3, \dots$ and λ_{+} (λ_{-}) is the wavelength of the RCP(LCP) wave *inside* the WSM. The WSM acts as a Fabry-Pérot interferometer in this situation.

E. Faraday and Kerr rotation and ellipticity angles

To compute the Faraday rotation and ellipticity angles for an incident linearly polarized wave with $\mathbf{e}_i = \hat{\mathbf{x}}$, we use Eqs. (73)-(74) to define the function η_F by

$$\eta_F = \frac{t\beta_t}{t\alpha_t} = -i \frac{A_+ - A_-}{A_+ + A_-}. \quad (85)$$

In the general case where the polarization of the transmitted wave is elliptical, the angle θ_F is defined as the angle that the major axis of the polarization ellipse makes with the direction of the incident (linear) polarization *i.e.* the x axis if $\mathbf{e}_i = \hat{\mathbf{x}}$. We use the following definition³⁰ for the Faraday rotation angle

$$\tan 2\theta_F = \frac{2 \operatorname{Re}[\eta_F]}{1 - |\eta_F|^2}, \quad (86)$$

where $\theta_F \in [-\pi/2, \pi/2]$. The major and minor axis of the ellipse have length a and g respectively. The ellipticity angle ψ_F is defined³⁰ as

$$\tan \psi_F = \pm \frac{g}{a}, \quad (87)$$

where the \pm signs indicate the direction of rotation of the electric field vector along the ellipse and $g/a \in [0, 1]$. Thus, a change in the sign of the ellipticity corresponds to a change in the direction of the rotation of the polarization vector on the ellipse. The ellipticity angle is given by the equation³⁰

$$\sin 2\psi_F = \frac{2 \operatorname{Im}[\eta_F]}{1 + |\eta_F|^2}. \quad (88)$$

A linear polarization corresponds to $\psi_F = 0$ while a circular polarization has $\psi_F = -\pi/4$ for RCP and $\psi_F = \pi/4$ for LCP (assuming forward propagation).

To compute the Kerr rotation and ellipticity angles of the reflected wave, we assume again that the incident wave is linearly polarized with $\mathbf{e}_i = \hat{\mathbf{x}}$. The corresponding η_K function is now

$$\eta_K = \frac{r\beta_r}{r\alpha_r} = -i \frac{C_+ - C_-}{C_+ + C_-}, \quad (89)$$

and thus we have

$$\tan 2\theta_K = \frac{2 \operatorname{Re}[\eta_K]}{1 - |\eta_K|^2}, \quad (90)$$

$$\sin 2\psi_K = \frac{2 \operatorname{Im}[\eta_K]}{1 + |\eta_K|^2}. \quad (91)$$

Because the direction of propagation is reversed, $\psi_F = \pi/4$ for RCP and $\psi_F = -\pi/4$ for LCP. For any other orientation θ_i of the polarization vector with respect to the x axis, one would need to subtract θ_i from θ_K to obtain the effective rotation angle $\theta_K - \theta_i$. By symmetry, this angle must be independent of θ_i in the Faraday configuration.

F. Thin film limit

In the thin film limit where the wavelength of the incident light $\lambda \gg d$, we have $\xi = 2.1 \times 10^{-3} \ll 1$ for $d = 100$ nm and $f = 2\pi/\omega = 10^{12}$ Hz. Thus, $\sin(n_{\pm}\xi) \approx n_{\pm}\xi$ and $\cos(n_{\pm}\xi) \approx 1$ in A_{\pm} and C_{\pm} . If we consider, in addition, that $n_1 = n_3$, we have the simple result

$$A_{\pm} \approx \frac{n_1}{(n_1^2 + \varepsilon_{\pm})\xi + 2in_1}. \quad (92)$$

The function $\eta_F \ll 1$ and so the Faraday and ellipticity angles are given by

$$\theta_F \approx \operatorname{Re}[\eta_F] \approx \operatorname{Re} \left[\frac{n\kappa b d}{2n_1 - i\xi(\varepsilon - \varepsilon_b)} \right], \quad (93)$$

$$\psi_F \approx \operatorname{Im}[\eta_F] \approx \operatorname{Im} \left[\frac{n\kappa b d}{2n_1 - i\xi(\varepsilon - \varepsilon_b)} \right]$$

or, to first order in d by

$$\theta_F \approx \frac{n\kappa b d}{2n_1}, \quad (94)$$

$$\psi_F \approx 0. \quad (95)$$

In this limit, the transmitted wave is linearly polarized and the Faraday rotation is directly proportional to the WSM width, the Chern number¹⁹ and the axion term b . We can define a rotating power by

$$R_0 = \frac{\partial \theta_F}{\partial d} = \frac{n\kappa b}{2n_1} = 0.23 \frac{nb}{n_1} \text{ mrad/nm}, \quad (96)$$

with b in units of 10^8 m^{-1} .

For the Kerr angle and with $n_1 = n_3$, we find in the thin film limit that

$$C_{\pm} \approx \frac{(n_1^2 - n_{\pm}^2)\xi}{(n_1^2 + n_{\pm}^2)\xi + 2in_1} \quad (97)$$

and so we have

$$\eta_K \approx \frac{2n_1}{\omega} \left[\frac{n\kappa b}{2in_1(\varepsilon - n_1^2) + \xi\varepsilon + \varepsilon_-} \right]. \quad (98)$$

However, the function η_K is not small in the frequency range considered in our calculations and so we cannot use the approximation $\theta_K \approx \operatorname{Re}[\eta_K]$ for the Kerr angle in this limit.

G. Semi-infinite WSM

The limit of a semi-infinite WSM can be easily obtained by replacing n_3 by $n_+(\omega)$ in the equations for the RCP mode and by $n_-(\omega)$ for the LCP mode. We get in this way

$$C_{\pm} = \frac{n_1 - n_{\pm}}{n_1 + n_{\pm}}, \quad (99)$$

so that

$$\eta_K = in_1 \frac{n_+ - n_-}{n_1^2 - n_+ n_-}. \quad (100)$$

The reflection coefficient is given by

$$R_{LCP} = \frac{1}{2} \left(\left| \frac{n_1 - n_+}{n_1 + n_+} \right|^2 + \left| \frac{n_1 - n_-}{n_1 + n_-} \right|^2 \right). \quad (101)$$

The function η_K is again not small to that the approximation $\theta_K \approx \text{Re}[\eta_K]$ is not valid. The Kerr effect for a semi-infinite WSM has been studied before. See, for example Ref. 13 for Chern number $n = 1$ and Ref. 21 for mWSMs.

We remark that changing the sign of the axion term b simply interchanges ε_+ and ε_- and so $T_{RCP} \longleftrightarrow T_{LCP}$ and $R_{RCP} \longleftrightarrow R_{LCP}$. The coefficients T_{LP} and R_{LP} do not change. The Faraday and Kerr rotation and ellipticity angles change sign.

V. NUMERICAL RESULTS

A. Dielectric functions

The real (full lines) and imaginary (dashed lines) parts of $\varepsilon(\omega)$ given by Eq. (5) for a WSM with two nodes of opposite chiralities and Chern number $n = 1$ is plotted in Fig. 1. Curve 1 (black) is $\varepsilon(\omega)$ with interband transitions only, curve 2 (blue) is $\varepsilon(\omega)$ with intraband transitions only and curve 3 (red) includes both types of transitions. We take $\tau = 100$ ps in our calculation to be in a low-disorder limit. This parameter depends on temperature and also on the material quality. We analyse its effect later on in this paper. Curve 4 (green) shows the effect of a finite b_0 and curve 5 (orange) shows $\varepsilon(\omega)$ in the absence of doping ($e_F = 0$). When $e_F \neq 0$, the real part of $\varepsilon(\omega)$ is positive with a logarithmic divergence at $\omega_{th} = 2e_F/\hbar$ (i.e. $f = 4.83 \times 10^{12}$ Hz in Fig. 1) which is the threshold for interband absorption. When intraband transitions are absent, the imaginary part of $\varepsilon(\omega)$ is strictly zero below this threshold because of the Pauli blocking. With intraband transitions considered, $\varepsilon(\omega)$ has a finite imaginary part which is very small except at low frequency. With a finite b_0 , the Weyl nodes are shifted in energy by $2\hbar b_0$ and there are two thresholds for absorption at $\omega_{th} \pm 2b_0$ as shown in Fig. 1. Intraband

transitions (curve 2) make the real part of $\varepsilon(\omega)$ negative when $\omega < \omega_p$ where ω_p is the plasmon frequency given for $\tau \rightarrow \infty$ by

$$\omega_p = \frac{2}{\hbar} \sqrt{\frac{n\alpha c (e_F^2 + \hbar^2 b_0^2)}{3\pi v_F}}, \quad (102)$$

when only intraband transitions are considered. This frequency scales with the square-root the of Chern number in this limit. The plasmon frequency is however red-shifted by the interband transitions as seen in curve 3. It is then given by the solution of the transcendental equation^{13,31}

$$\omega_p = \sqrt{\frac{4n\alpha c}{3\pi\hbar^2 v_F} \frac{e_F^2 + \hbar^2 b_0^2}{\beta(\omega_p)}}, \quad (103)$$

where

$$\beta(\omega) = 1 + \frac{n\alpha}{6v_F/c} \sum_x \frac{1}{\pi} \ln \left(\left| \frac{\omega^2 - 4v_F^2 k_c^2}{\omega^2 - 4e_{F,x}^2} \right| \right). \quad (104)$$

We remark in passing that the contribution of the terms that do not contain $e_{F,x}$ in the intraband part of ε in Eq. (5) is negligible in the clean limit.

When interband transitions only are considered (curve 1) an electromagnetic wave (EMW) can propagate in the WSM with zero attenuation if $\omega < \omega_{th}$. Intraband transitions introduce a region $\omega < \omega_p$ where the EM wave is evanescent. For sufficiently large τ , and with $b = 0$, the EMW can propagate with almost no dissipation in the region $\omega \in [\omega_p, \omega_{th}]$. When $e_F = 0$, the EMW propagates at all frequencies but with some dissipation (curve 5).

In a mWSM, the conductivity tensor is multiplied by the Chern number n as indicated by Eq. (5). It follows that, when intraband transitions only are considered, the plasmon frequency scales with \sqrt{n} as indicated in Eq. (102). But, when the correction $\beta(\omega)$ is considered, the plasmon frequency becomes almost independent of the Chern number. Indeed, as shown by curve 6 in Fig. 1, the position of the zero of $\text{Re}[\varepsilon(\omega)]$ for $n = 3$ is very close to the zero of $\text{Re}[\varepsilon(\omega)]$ for $n = 1$.

When the axion term $\mathbf{b} \neq 0$, the propagation of the electromagnetic wave depends on the dielectric functions $\varepsilon_{\pm}(\omega)$ defined by Eqs. (21) and (22). When $\varepsilon_F \neq 0$, $\varepsilon(\omega)$ is finite at $\omega = 0$. In the $\omega \rightarrow 0$ limit, the asymptotic behavior of $\varepsilon_{\pm}(\omega)$ is governed by the sign of the axion term i.e. $\varepsilon_{\pm}(\omega \rightarrow 0) \rightarrow \pm\infty$ when b is positive. In this paper, however, we concern ourselves with the behavior of the transmission and Faraday rotation in the THz frequency domain.

The real (full lines) and imaginary (dashed lines) parts of the refractive indices $n_{\pm}(\omega)$ are plotted in Fig. 2 where we have taken $e_F = 10$ meV, $b = 1$, $b_0 = 0$, $\tau = 100$ ps and $n = 1$. Curve 1, however, has $b = 0$ in order to indicate the position of the plasmon frequency. Curve 2 is for $n_-(\omega)$ and curve 3 for $n_+(\omega)$. The corresponding

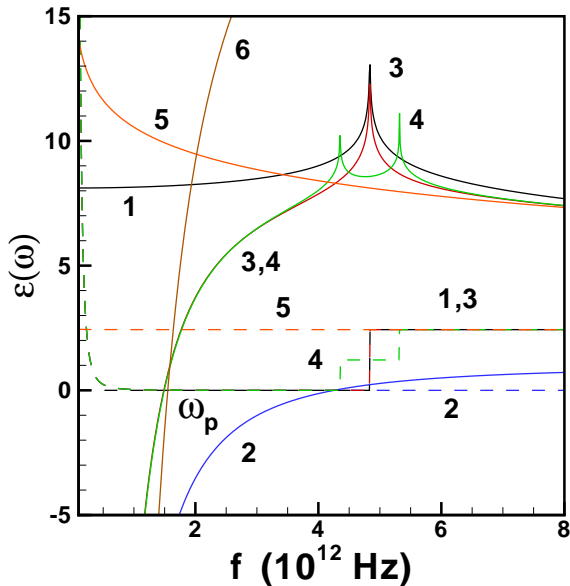


FIG. 1. Fig. 1 Real (full lines) and imaginary (dashed lines) parts of the dielectric function $\varepsilon(\omega)$ of a WSM as a function of frequency for: (1) [black] interband transitions only, $e_F = 10$ meV, $b_0 = 0$; (2) [blue] intraband transitions only $e_F = 10$ meV, $b_0 = 0$; (3) [red] both transitions, $e_F = 10$ meV, $b_0 = 0$; (4) [green] both transitions $e_F = 10$ meV, $b_0 = 1$ meV; (5) [orange] both transitions, $e_F = 0$ meV, $b_0 = 0$; 6 [brown] both transitions, portion of the real part of $\varepsilon(\omega)$ for $e_F = 10$ meV, $b_0 = 0$ and Chern number $n = 3$. Other parameters are $\varepsilon_b = 1$, $v_F = 3 \times 10^5$ m/s, $k_c = 50 \times 10^8$ m $^{-1}$ and $\tau = 100$ ps.

dielectric functions are zero at ω_+ and ω_- in the clean limit. These two frequencies are defined by the solution of the transcendental equation

$$\omega_{\pm} = \frac{\mp c\kappa b}{\varepsilon(\omega_{\pm})}. \quad (105)$$

We find that $\omega_+ < \omega_p$ and $\omega_- > \omega_p$. The refractive indices $n_+(\omega)$ and $n_-(\omega)$ govern the propagation of the F-RCP and F-LCP waves respectively. When $\omega < \omega_+$, the F-RCP wave is evanescent and cannot propagate while for $\omega \in [\omega_+, \omega_{th}]$ it propagates with almost no dissipation (in the low-disorder limit). For $\omega > \omega_{th}$, the F-RCP wave propagates with some dissipation as the refractive index is complex. The same scenario occurs for the F-LCP wave with ω_+ replaced by ω_- . The frequency range where the F-LCP wave propagates with almost no dissipation is smaller than that of the F-RCP wave.

The lines in Fig. 3 indicate the boundaries of the propagating regions $[\omega_+, \omega_{th}]$ and $[\omega_-, \omega_{th}]$ for the F-RCP and F-LCP waves when $b = 1 \times 10^8$ m $^{-1}$ and $b = 5 \times 10^8$ m $^{-1}$. Below ω_+ or ω_- , the corresponding wave is evanescent. Above ω_{th} , both waves propagate but with some dissipation. These frequency ranges are modified by a change in the Fermi level and axion term b . Increasing b increases the frequency range for the F-RCP wave and decreases

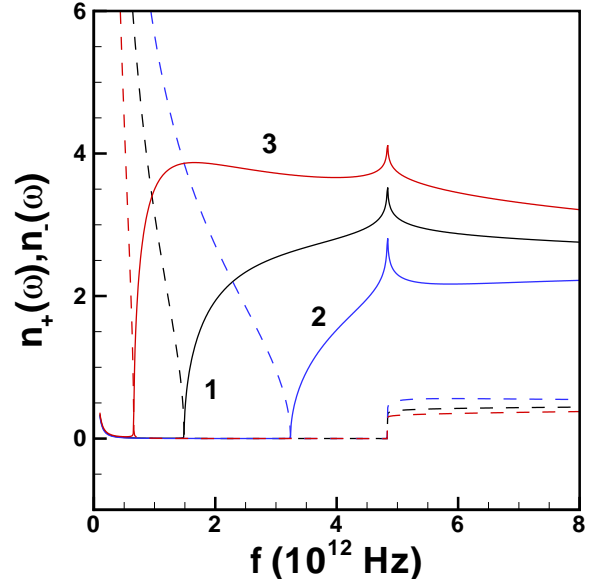


FIG. 2. Real (full lines) and imaginary part (dashed lines) of the refractive indices $n_+(\omega)$ and $n_-(\omega)$ as a function of frequencies. Curve 1 [black] $n_{\pm}(\omega)$, $b = 0$; 2 [blue] $n_-(\omega)$ for $b = 1 \times 10^8$ m $^{-1}$; 3 [red] $n_+(\omega)$ for $b = 1 \times 10^8$ m $^{-1}$. Other parameters are $\varepsilon_b = 1$, $\tau = 100$ ps, $b_0 = 0$, $e_F = 10$ meV, $k_c = 50 \times 10^8$ m $^{-1}$ and $n = 1$.

that of the F-LCP wave. If intraband transitions are neglected (the situation considered in Ref. 16), then ω_- is slightly redshifted while $\omega_+ \rightarrow 0$ so that the RCP wave can propagate without dissipation in the whole frequency range $\omega \in [0, \omega_{th}]$.

B. Transmission of circularly polarized waves

We consider that the incident wave is either RCP or LCP polarized. We use the same parameters as in Fig. 2 *i.e.* $e_F = 10$ meV, $\varepsilon_b = 1$, $b_0 = 0$, $b = 1 \times 10^8$ m $^{-1}$ and $\tau = 100$ ps and assume a width $d = 30 \mu\text{m}$ for the WSM. For the two dielectrics, we take $n_1 = n_3 = 1$ unless specified otherwise. The wavelength of the F-RCP and F-LCP waves inside the WSM is, from Eqs. (21) and (22), given by

$$\lambda_+ = \lambda_{F-RCP} = 2\pi / \text{Re}[q_{1+}], \quad (106)$$

$$\lambda_- = \lambda_{F-LCP} = 2\pi / \text{Re}[q_{2+}]. \quad (107)$$

Figure 4 shows the transmission coefficients T_{RCP} and T_{LCP} and the ratios d/λ_+ and d/λ_- . The onsets of propagation occurs at $d/\text{Re}[\lambda_{\pm}] = 0$ which corresponds to the frequencies ω_{\pm} . The logarithmic divergence in d/λ_{\pm} signals the absorption edge at ω_{th} . As discussed previously, the RCP and LCP waves propagate with almost no attenuation in the frequency range $\omega = [\omega_+, \omega_{th}]$ for the RCP wave and $\omega = [\omega_-, \omega_{th}]$ for the LCP wave. Above

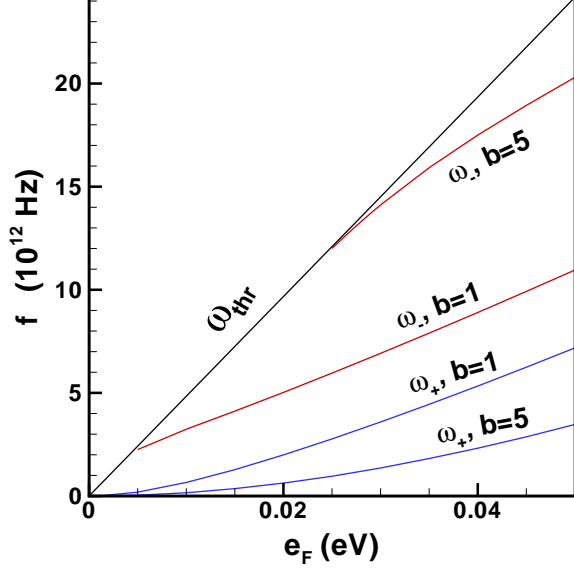


FIG. 3. Behavior with Fermi level of the boundary of the different propagating regions identified in Fig. 2 for two values of the axion term: $b = 1 \times 10^8 \text{ m}^{-1}$ and $b = 5 \times 10^8 \text{ m}^{-1}$. Other parameters are $n = 1$, $\tau = 100 \text{ ps}$, $\varepsilon_b = 1$, $b_0 = 0$, $k_c = 50 \times 10^8 \text{ m}^{-1}$.

ω_{th} , the waves propagate but are attenuated while below ω_{\pm} , they are evanescent. There is a small but finite transmission even with evanescent waves if d is not too big. The transmission is finite and sizeable for each polarization when $\omega_{\pm} < \omega < \omega_{th}$. In these frequency ranges, there is a series of transmission resonances which occur whenever $\cos(n_{\pm}\xi) = 1$ in A_{\pm} [Eqs. (51) and (63)] *i.e.* whenever the quantization condition given by Eq. (83) is satisfied. If the refractive indices $n_{\pm}(\omega)$ are real, the transmission at these resonances is maximal *i.e.* $T = 1$. This maximal value is achieved when intraband transitions are neglected since they are the only source of dissipation in our model. The transmission drops abruptly when $\omega > \omega_{th}$.

Since b determines in part the frequencies ω_{\pm} , it follows that the frequency range $\omega \in [\omega_{\pm}, \omega_{th}]$ in which the RCP and LCP waves propagate can be tuned by changing b as was noticed before¹⁶. For example, if b is increased to $b = 2.5 \times 10^8 \text{ m}^{-1}$ with the parameters of Fig. 4, only the RCP wave can be transmitted below the absorption edge. With $b = -2.5 \times 10^8 \text{ m}^{-1}$, the converse is true and it is the RCP wave that is blocked. It is thus possible, in principle, to filter out the LCP wave from an incident LP wave in a broad range of frequencies by changing \mathbf{b} . It has recently been shown³² that a large enhancement of this axion term by a factor of four can be achieved in the Weyl semimetal Cd_3As_2 by strain tuning.

In the frequency range $\omega \in [\omega_+, \omega_-]$, the RCP wave can propagate only forward and not backward so that a

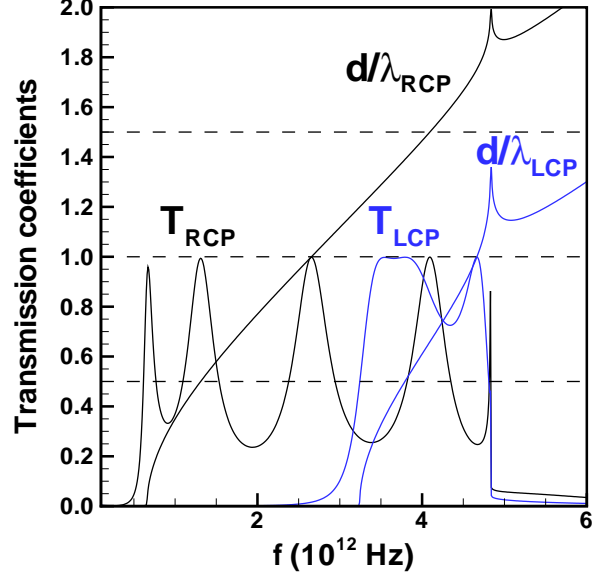


FIG. 4. Transmission coefficients T_{RCP} and T_{LCP} and ratios d/λ_{RCP} and d/λ_{LCP} as a function of frequency for an incident RCP or LCP wave. Parameters are $n = 1$, $e_F = 10 \text{ meV}$, $b_0 = 0$, $\tau = 100 \text{ ps}$, $\varepsilon_b = 1$, $d = 30 \mu\text{m}$, $k_c = 50 \times 10^8 \text{ m}^{-1}$, $n_1 = n_3 = 1$, and $b = 1 \times 10^8 \text{ m}^{-1}$. The horizontal dashed lines are set at $m/2$ where $m = 1, 2, 3, \dots$. They indicate frequencies at which the quantization condition is satisfied.

WSM can also act as a broadband optical isolator¹⁶.

As seen in Fig. 3, increasing the Fermi level e_F for a fixed b value increases ω_+ . It is thus possible to increase the region where both waves are blocked ($\omega < \omega_+$) by increasing the doping. The Fermi level can be tuned by electric gating or by changing the temperature¹⁹.

From Eq. (23), we see that increasing $|b|$ increases the refractive index $n_+(\omega)$ thus decreasing the wavelength $\lambda_+(\omega)$ and making the transmission coefficient $T_{RCP}(\omega)$ oscillates more rapidly while decreasing the threshold frequency ω_+ for the onset of propagation. Increasing $|b|$ has the opposite effect on $n_-(\omega)$.

We find numerically that increasing the Chern number increases both refractive indices, making the oscillations more rapid and decreasing ω_{\pm} .

C. Transmission of a linearly polarized wave and Faraday rotation

The effect of the axion term b on the transmission coefficient T_{LP} of a linearly polarized (LP) wave is shown in Fig. 5. A linearly polarized wave can be written as a sum of a RCP and a LCP waves of equal amplitude and phase. When $\omega \in [\omega_+, \omega_-]$, only the RCP portion of the LP wave is transmitted and, since the attenuation is very small for $\tau = 100 \text{ ps}$, the maximal transmission

reaches $T_L = 0.5$ at ω_+ and subsequently at all the transmission resonances in this frequency range. Figure 5 also shows the Faraday ellipticity angle. It is $\psi_F = -\pi/4$ in $\omega \in [\omega_+, \omega_-]$ so that the transmitted wave is RCP as expected. In $\omega \in [\omega_-, \omega_{th}]$, both circular polarizations are transmitted but with unequal amplitude. The oscillatory pattern for T_{LP} is then more complex. The transmission reaches $T_{LP} = 1$ when the quantization condition given by Eq. (83) is satisfied by the two waves (with different values of m for the RCP and LCP components). When $T_{LP} = 1$ in $\omega \in [\omega_-, \omega_{th}]$, the transmitted wave has $\psi_F = 0$ and is linearly polarized. At other frequencies in this frequency range, the polarization is elliptical. Hence, the WSM can act as a RCP polarizer, in some frequency range below ω_{th} if $b > 0$ or as a LCP polarizer if the orientation of the WSM is reversed making $b < 0$.

Above ω_{th} , we can define a meaningful Faraday angle θ_F although the polarization is very close to being circular. The Faraday rotation is substantial and increases with frequency while there is simultaneously little change in the ellipticity angle ψ_F . The transmission coefficient, however, is close to zero. A bigger transmission coefficient is obtained by reducing the width of the WSM. This also kills the oscillations. At $f = 10^{12}$ Hz, the wavelength of light in vacuum is $\lambda = 300\mu\text{m}$. If we choose $d = 1\mu\text{m}$, then the quantization condition for the transmission resonances is not satisfied. Figure 6 shows the transmission coefficient T_{LP} , ellipticity and Faraday angles for an incident linearly polarized wave in this limit with $b_0 = 0$ (full lines) and $\hbar b_0 = 1$ meV (dashed lines). The transmitted wave is elliptically polarized. The Faraday rotation angle and the transmission are large in a broad range of frequencies. A finite b_0 creates a logarithmic singularity in T_{LP} , θ_F and ψ_F at the absorption thresholds $\omega_{th} \pm 2b_0$ in Fig. 6. From a measure of the transmission coefficient, one could thus determine the energy shift between the two nodes.

In the thin-film limit, Eq. (93) shows that the Faraday and ellipticity angles scale linearly with b . Without loss of generality, we can thus choose a frequency $f = 4 \times 10^{12}$ Hz from Fig. 6 and plot the Faraday angle as a function of the width d of the slab of WSM. The resulting graph is shown in Fig. 7 for Chern number $n = 1, 2, 3$. The Faraday angle increases linearly with d at a rate of $R_0 = \partial\theta_F/\partial d \approx 0.21$ mrad/nm for $n = 1$. This is exactly what Eqs. (85) and (86) give in the thin film limit $\lambda \gg d$. Indeed, at $f = 4 \times 10^{12}$ Hz and for $d = 100$ nm, Eq. (44) gives $\xi = 0.002$ and Fig. 3 shows that $n_+ \approx 4$ and $n_- \approx 2$ so that we are justified to take $\cos(n_{\pm}\xi) \approx 1$ and $\sin(n_{\pm}\xi) \approx n_{\pm}\xi$ in Eq. (51) and Eq. (63). The Faraday angle is thus given by Eq. (93) (represented by the square symbols in Fig. 7). At very small d , a good fit is obtained by Eq. (94) *i.e.* $\theta_F \approx n\kappa b d/2n_1$. The rotating power that we obtain is $R_0 \approx 0.21$ mrad/nm for $n = 1$, not far from what was recently measured³³ in a thin film of the magnetic WSM Co_2MnGa where $R_0 \approx 3$ mrad/nm. A Faraday angle of $\theta_F = 100$ mrad giving $R_0 \approx 2.4$ mrad/nm was also reported³⁴ for a thin film

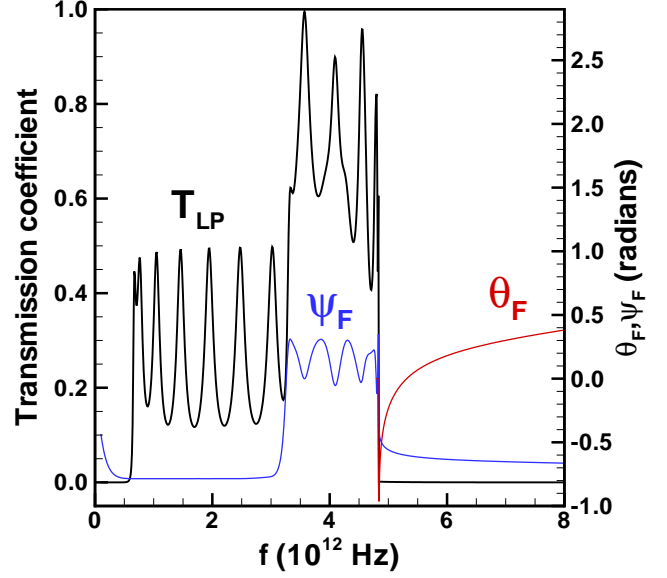


FIG. 5. Transmission coefficient T_{LP} and Faraday ellipticity ψ_F and rotation angle θ_F as a function of frequency for an incident linearly polarized wave. Parameters are $n = 1$, $e_F = 10$ meV, $b_0 = 0$, $\tau = 100$ ps, $n_1 = n_3 = 1$, $\varepsilon_b = 1$, $k_c = 50 \times 10^8$ m^{-1} , $b = 1 \times 10^8$ m^{-1} and $d = 80\mu\text{m}$.

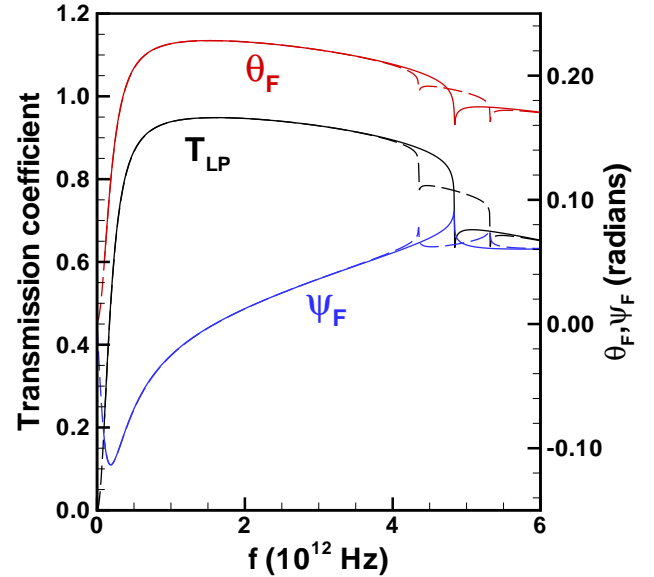


FIG. 6. Transmission coefficient T_{LP} , ellipticity angle ψ_F and Faraday angle θ_F for an incident linearly polarized wave as a function of frequency. Parameters are $n = 1$, $e_F = 10$ meV, $\tau = 100$ ps, $\varepsilon_b = 1$, $n_1 = n_3 = 1$, $b = 1 \times 10^8$ m^{-1} , $k_c = 50 \times 10^8$ m^{-1} and $d = 1\mu\text{m}$. Full lines: $b_0 = 0$, dashed lines: $\hbar b_0 = 1$ meV.

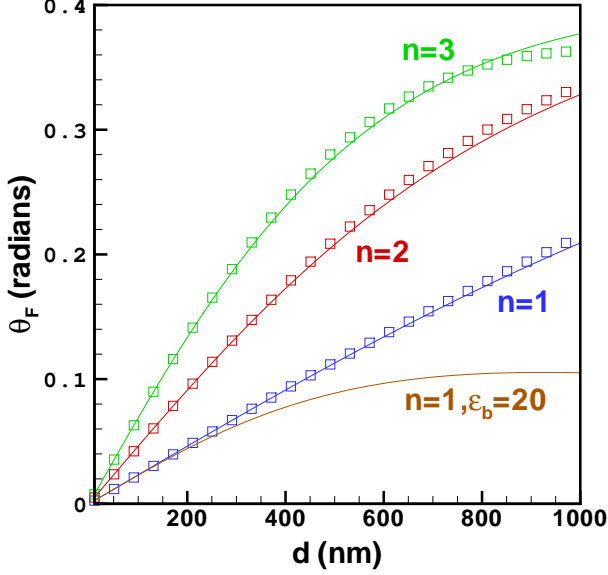


FIG. 7. Faraday angles as a function of the width d of the Weyl semimetal for Chern number $n = 1, 2, 3$ for an incident linearly polarized wave at frequency $f = 4 \times 10^{12}$ Hz. The full lines are the exact results while the thin film limit given by Eq. (93) is represented by the square symbols. Parameters are $e_F = 10$ meV, $b_0 = 0$, $\tau = 100$ ps, $b = 1 \times 10^8$ m $^{-1}$, $n_1 = n_3 = 1$ and $\varepsilon_b = 1$. The [brown] curve labeled $n = 1, \varepsilon_b = 20$ shows the effect of increasing the background dielectric constant to $\varepsilon_b = 20$.

($d = 42$ nm), of another magnetic WSM: $\text{Co}_3\text{Sn}_2\text{S}_2$ (see Ref. 35 for a review of its properties). This was considered as a large value by these authors when compared with the conventional magneto-optical material Bi:YIG which has $R_0 = 0.77$ mrad/nm 34 . In yet another WSM 36 , Co_2TiGe , the measured Faraday angle was $\theta_F \approx 0.012$ rad for a width $d = 72$ nm giving $R_0 \approx 0.17$ mrad/nm. Although these three WSM have different parameters, the measured Faraday angles are of the same order of magnitude. Figure 7 shows that the range of d where the linear approximation [Eq. (94)] holds decreases with the Chern number.

Since the background dielectric constant ε_b can be much greater than 1 in some WSMs, we also plot, in Fig. 7, the Faraday angle for $\varepsilon_b = 20$ and $n = 1$. As expected, increasing ε_b decreases the Faraday rotation angle at larger d and reduces the region where the linear relation is valid. This parameter has no effect in the linear region where Eq. (94) holds.

Another way to control the transmitted signal is to change the dielectrics in regions 1 and 3. Figure 8 shows that the oscillations in the region $\omega \in [\omega_+, \omega_-]$ where only the RCP wave is transmitted are completely suppressed by taking $n_1 = n_3 = 4$ (curve 3) which is, according to Fig. 3, the value that matches the dielectric constant $n_+(\omega)$ in this frequency range. The suppression of these

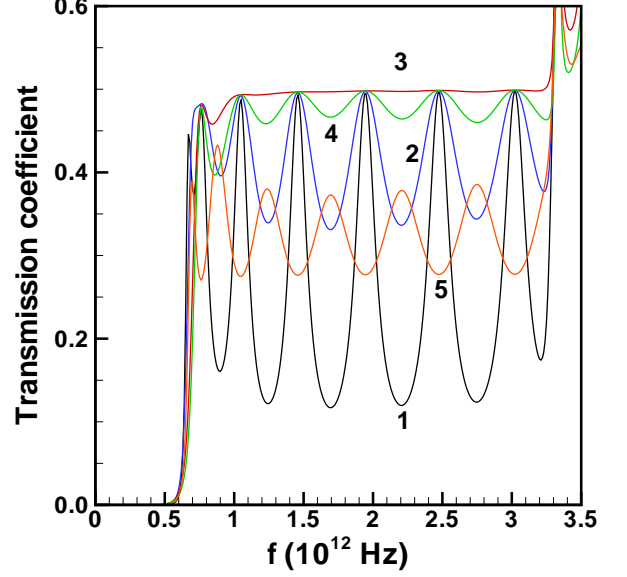


FIG. 8. Effect of the dielectric constants n_1 and n_3 on the oscillatory pattern of the transmission coefficient T_{LP} in the region where only the RCP wave propagates. Parameters are $e_F = 10$ meV, $b_0 = 0$, $\tau = 100$ ps, $b = 1 \times 10^8$ m $^{-1}$, $k_c = 50 \times 10^8$, $\varepsilon_b = 1$, m $^{-1}$ and $d = 80$ μm . The first four curves are for $n_1 = n_3$ with (1) $n_1 = 1$; (2) $n_1 = 2$; (3) $n_1 = 4$; (4) $n_1 = 5$ and curve (5) has $n_1 = 1, n_3 = 5$.

oscillations is easily understood. When $n_+ = n_1 = n_3$ in Eq. (53), the coefficients of the forward and backward propagating waves in the WSM are $t_1 = 1$ and $t_2 = 0$ so that $A_+ = 1/2$ and $T_{LP} = 1/2$. Since $t_2 = 0$ there is no reflected wave, consistent with the fact that there is no discontinuity in the dielectric constant at the two interfaces. As discussed in Sec. 4(d), the maxima of transmission in the first four curves in Fig. 8 are given by the condition $\cos^2(n_+\xi) = 1$. Curve 5 has $n_1 = 1, n_3 = 5$ and satisfies the criteria $n_+ \in [n_1, n_3]$ so that the transmission maxima are given by $\sin^2(n_+\xi) = 1$ and so shifted by half a period of oscillation.

Figure 9 shows the threshold frequency $f_+ = \omega_+/2\pi$ for the propagation of an RCP wave as a function of the Fermi level for different values of the parameters n, ε_b and cutoff wave vector k_c . The RCP wave propagates with almost no dissipation in the range $\Delta = [\omega_+, \omega_{th}]$. The frequency ω_{th} is represented by curve 1. Curve 2 shows ω_+ and so Δ for $\varepsilon_b = 1, v_F/c = 0.001, k_c = 50 \times 10^8$ m $^{-1}, n = 1, e_F = 10$ meV, $b_0 = 0, \tau = 100$ ps. With respect to curve 2, the other curves show how Δ is modified by changing one parameter. Curve 3 shows the effect of changing k_c to $k_c = 50 \times 10^8$ m $^{-1}$ and curve 4 that of taking $n = 2$. Curve 5 has $\varepsilon_b = 20$ and curve 6 has $v_F/c = 0.003$.

The scattering time τ depends on the temperature and on the quality of the material. We have so far considered

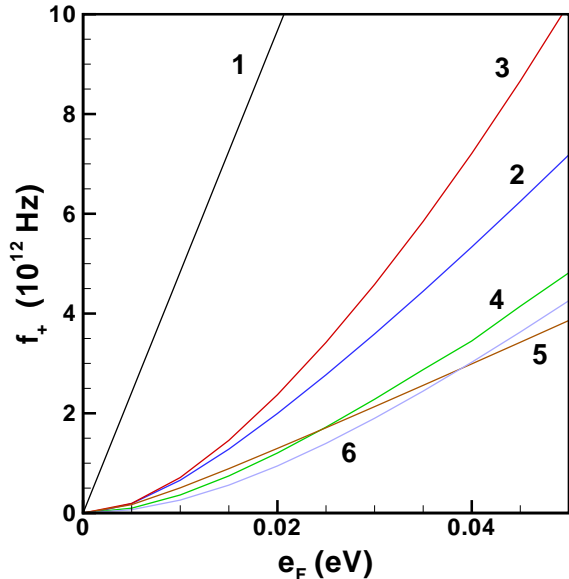


FIG. 9. Effect of different parameters on the propagation range of an RCP wave in the WSM. Curve 1 is the absorption edge frequency $\omega_{th}/2\pi$. The other curves give $f_+ = \omega_+/2\pi$ for : (2) $n = 1, \varepsilon_b = 1, k_c = 50 \times 10^8 \text{ m}^{-1}$; (3) $n = 1, \varepsilon_b = 1, k_c = 5 \times 10^8 \text{ m}^{-1}$; (4) $n = 2, \varepsilon_b = 1, k_c = 50 \times 10^8 \text{ m}^{-1}$; (5) $n = 1, \varepsilon_b = 20, k_c = 50 \times 10^8 \text{ m}^{-1}$; (6) $n = 1, \varepsilon_b = 1, k_c = 50 \times 10^8 \text{ m}^{-1}, v_F/c = 0.003$. Other parameters are $e_F = 10 \text{ meV}$, $b_0 = 0, \tau = 100 \text{ ps}$, $b = 1 \times 10^8 \text{ m}^{-1}$ and (for curves 1-5) $v_F/c = 0.001$.

the pure limit with $\tau = 100 \text{ ps}$, but τ can be substantially smaller. For example, in Co_2TiGe , it is reported³⁶ to be $\approx 0.15 \text{ ps}$, in $\text{Co}_3\text{Sn}_2\text{S}_2$ it is $\approx 0.22 \text{ ps}$ ³⁴ and in Co_2MnGa it is $\approx 0.22 - 0.33 \text{ ps}$ ³³. (These results are for finite temperature.) It is thus important to see how a variation of this parameter influences the transmission. Figure 10 shows the effect of varying the scattering time τ on the oscillatory pattern of the transmission coefficient for the RCP wave. The different curves, in order of decreasing amplitude are for $\tau = 100$ (black), 10 (blue), 1 (red) and 0.1 ps (green). The reduction in the transmission amplitude becomes really important when τ is of the order of a picosecond or smaller. When $\tau < 0.1$, we find numerically that there is no crossing between $\text{Re}[\varepsilon_+(\omega)]$ and the frequency axis so that the region where the wave is evanescent disappears and the wave can propagate but with some dissipation. In fact, when $\tau > 0.1 \text{ ps}$, $\text{Re}[q_{1\pm}] \ll \text{Im}[q_{1\pm}]$ in the frequency range where the RCP wave is blocked while it is the opposite if $\tau < 0.1 \text{ ps}$. This explains the increase in the transmission coefficient at low frequency for $\tau = 0.1 \text{ ps}$ in Fig. 10.

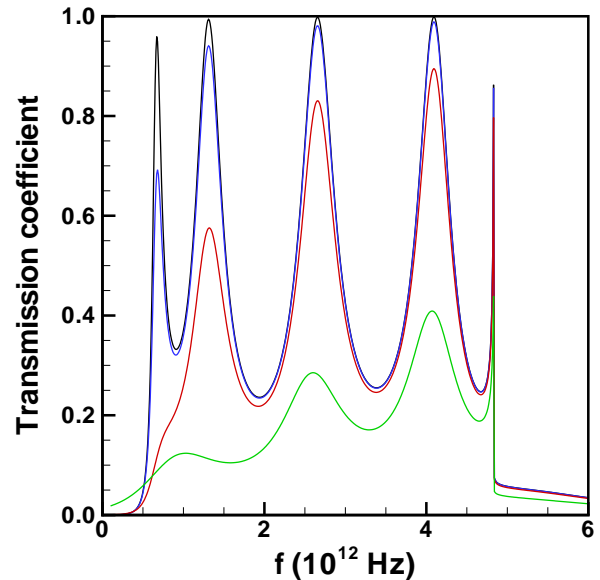


FIG. 10. Effect of the scattering time τ on the transmission coefficient T_{RCP} . In order of decreasing amplitude: [black] $\tau = 100 \text{ ps}$ [blue] $\tau = 10 \text{ ps}$; [red] $\tau = 1 \text{ ps}$; [green] $\tau = 0.1 \text{ ps}$. Parameters are $n = 1, e_F = 10 \text{ meV}, b_0 = 0, b = 1 \times 10^8 \text{ m}^{-1}, k_c = 50 \times 10^8, \varepsilon_b = 1, m^{-1}, n_1 = n_3 = 1$, and $d = 30 \mu\text{m}$.

D. Reflection of a linearly polarized wave and Kerr rotation

We now study the behavior of the reflection coefficient and Kerr rotation and ellipticity angles in a WSM. Figure 11 shows the reflection coefficient for a linearly polarized wave, R_{LP} and the Kerr rotation angle θ_K for a thin slab of a WSM with thickness $d = 100 \text{ nm}$, axion term $b = 1 \times 10^8 \text{ m}^{-1}$ and for Chern number $n = 1, 2, 3$ as indicated. Between the two large steps in θ_K , the Kerr angle is close to $\theta_K = -\pi/2$ and the reflection coefficient is almost zero. We find numerically, for the parameters used in this figure, that the first discontinuity in θ_K occurs at the frequency ω_+ and the second at $\varepsilon_-(\omega) = 1$ while the discontinuity at $f \approx 5 \times 10^{12} \text{ Hz}$ is at the threshold frequency for optical absorption. The calculated ellipticity (not shown) indicates that the reflected wave is elliptically polarized in this frequency range. There is clearly a dependency of the Kerr angle on the Chern number in this thin film limit. Indeed, Fig. 12 shows the behavior of the Kerr angle at small frequency for the same parameters as in Fig. 11. In the region where θ_K is flat, we have clearly that $\theta_{K,n}$ for $n = 2, 3$ is given by $n\theta_{K,n=1}$.

In the clean limit, Fig. 6 above shows that the transmission coefficient for the RCP wave in the thin-film limit is almost 1 for $\omega < \omega_{th}$. The reflection coefficient is thus given by $R_{RCP} = 1 - T_{RCP}$ for $\omega < \omega_{th}$ in the clean limit so that the oscillations in R_{RCP} are in antiphase with those of T_{RCP} . The same behavior applies to the

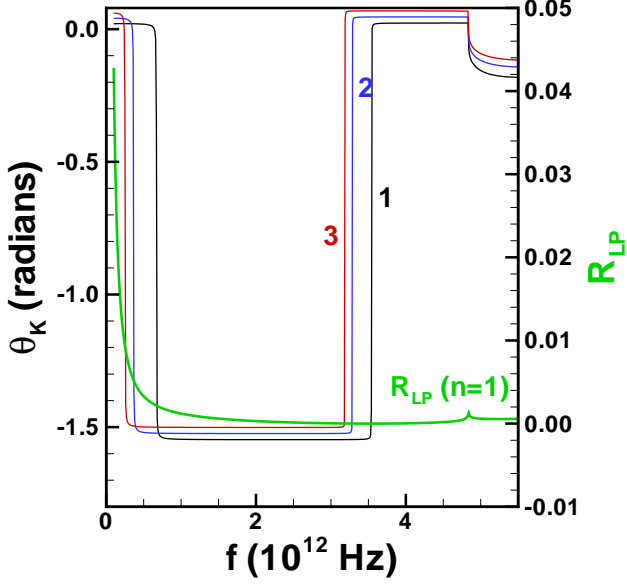


FIG. 11. Reflection coefficient R_{LP} and Kerr angle θ_K as a function of frequency and for Chern number $n = 1, 2, 3$ for a thin slab of a WSM with thickness $d = 100$ nm. Parameters are $e_F = 10$ meV, $b_0 = 0$, $\tau = 100$ ps, $b = 1 \times 10^8$ m $^{-1}$, $k_c = 50 \times 10^8$, $\varepsilon_b = 1$, m $^{-1}$, $n_1 = n_3 = 1$. The reflection coefficient shown is for $n = 1$.

LCP and LP waves. For $\omega > \omega_{th}$, however, the dissipation is important and $T + R < 1$.

In Fig. 13, we show the Kerr rotation angle $\theta_K(\omega)$ for Chern number $n = 1, 2, 3$ for reflection on a semi-infinite WSM. We use the function η_K given by Eq. (100) for this graph since the exact formula would give an infinite number of oscillations. The Kerr rotation angle is again quite large and clearly dependent on the Chern number.

Figure 14 shows the Kerr rotation and ellipticity angles and the reflection coefficient for $n = 1$ for the parameters used in Fig. 13. We find numerically, for the parameters used in this figure, that the first discontinuity in θ_K occurs at ω_+ and the second at ω_- *i.e.* at the threshold frequencies for the propagation of the RCP and LCP waves. The discontinuity at $f \approx 5 \times 10^{12}$ Hz is at the threshold frequency for optical absorption. When $\omega_- < \omega < \omega_{th}$, the dielectric functions ε_{\pm} are real and positive with a negligible imaginary part so that $\text{Re}[\eta_K] = 0$. The frequency ω^* in Fig. 14 corresponds to the condition $n_- = n_1$. Equation (100) gives in this case $\eta_K = -i$ and so $|\eta_K| = 1$. When $\omega_- < \omega < \omega^*$, we find that $|\eta_K| > 1$ and Eq. (90) gives $\theta_K(\omega) = -\pi/2$. For $\omega^* < \omega < \omega_{th}$, we have $|\eta_K| < 1$, and Eq. (90) then gives $\theta_K(\omega) = 0$. The reflection coefficient is important in this situation so that the Kerr angle is measurable. The ellipticity changes wildly at ω_{\pm} and ω^* . We remark that we have chosen our parameters for the Kerr angle in this section such that $\omega_+, \omega_- < \omega_{th}$. The Kerr angle $\theta_K(\omega)$

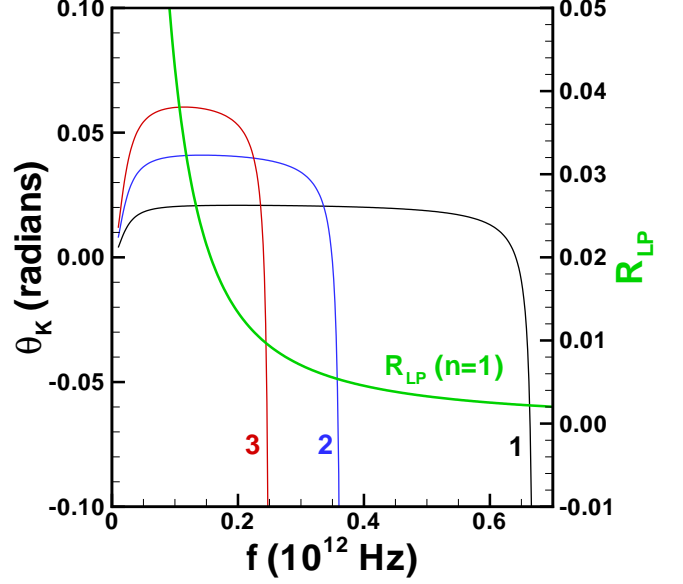


FIG. 12. Reflection coefficient R_{LP} and Kerr angle θ_K at low frequency for Chern number $n = 1, 2, 3$ for a thin slab of a WSM with thickness $d = 100$ nm. The parameters are those of Fig. 11. The reflection coefficient is shown for $n = 1$.

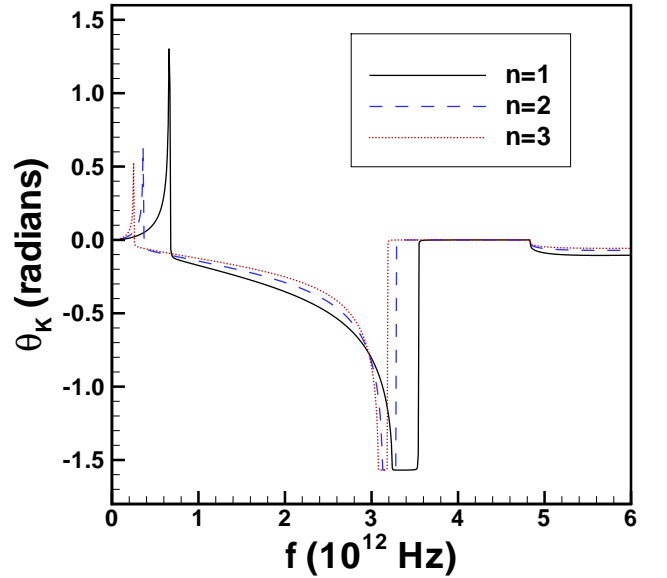


FIG. 13. Kerr angle $\theta_K(\omega)$ as a function of frequency for reflection on a semi-infinite WSM for Chern number $n = 1, 2, 3$. Parameters are $e_F = 10$ meV, $b_0 = 0$, $\tau = 100$ ps, $b = 1 \times 10^8$ m $^{-1}$, $k_c = 50 \times 10^8$, $\varepsilon_b = 1$, m $^{-1}$, $n_1 = n_3 = 1$.

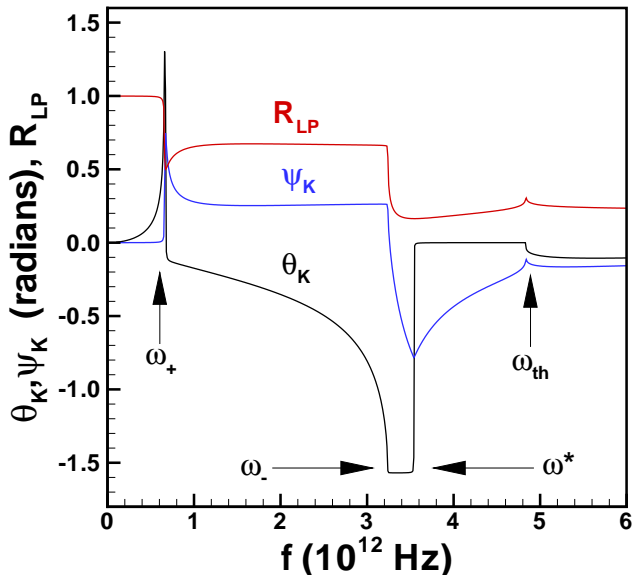


FIG. 14. Kerr rotation and ellipticity angles θ_K, ψ_K and reflection coefficient R_{LP} as a function of frequency for reflection on a semi-infinite WSM. Parameters are $n = 1$, $e_F = 10$ meV, $b_0 = 0$, $\tau = 100$ ps, $b = 1 \times 10^8$ m $^{-1}$, $k_c = 50 \times 10^8$, $\varepsilon_b = 1$, m $^{-1}$, $n_1 = n_3 = 1$.

would be different if, for example, $\omega_+ < \omega_{th} < \omega_-$ as shown in Ref. 13.

VI. CONCLUSION

The Maxwell equations that govern the propagation of electromagnetic waves inside a Weyl semimetal with broken time-reversal and space inversion symmetries are modified by the presence of the axion terms \mathbf{b} and b_0 . When light is incident on the surface of a WSM with no Fermi arcs and propagates in the direction of the vector \mathbf{b} , the right and left circular polarization experience different refractive indices. Hence, they propagate with different speeds and attenuation. The threshold frequency for their propagation is also different. (The waves are evanescent below the threshold frequency.) The axion term \mathbf{b} (and to some lesser extent b_0) also confers a gyrotropic nature to a WSM so that a linearly polarized wave will experience a rotation of its polarization vector upon reflection (Kerr effect) or transmission (Faraday effect)^{12,15–18}. Thus, at a fundamental level, a WSM is non-reciprocal medium with birefringent and dichroic characters even in the absence of an external magnetic field. At a practical level, WSMs can be used to make optical devices that act as chiral filters or polarizers or as optical isolators¹⁹ since, in this later case, it is possible to block the transmission of the RCP or LCP waves in a broad range of frequencies.

In this paper, we made an in-depth study of these effects by analyzing in detail how the different parameters that characterize a WSM control these unique optical properties. Working with a simple two-node model, but allowing for the Chern number of the two nodes to be $n = 1, 2, 3$, we studied the transmission, reflection and Kerr and Faraday effects for light incident on a thin film, a slab or a semi-infinite WSM. In a slab, there is the additional effect that the multiple reflections inside the WSM lead to transmission resonances at some quantized frequencies. The WSM then acts as a Fabry-Pérot interferometer. We have considered the following parameters in our study: axion terms, Fermi level (doping), Fermi velocity, Chern number, width of the WSM, relaxation time for intraband scattering, size of the high-energy cut-off, background dielectric constant and refractive indices of the dielectrics on both sides of the slab of WSM.

We limited our study to zero temperature. A finite temperature will change the Fermi level and therefore the numerical values of the different threshold frequencies that control the propagation of the electromagnetic waves inside the WSM. We did not consider a tilting of the Weyl nodes. Its effects have been studied extensively in the past years and more recently in multi-WSMs^{21,27,37–39}.

The Faraday configuration that we studied in this paper is associated with the circularly polarized waves. In the Voigt configuration where the propagation is perpendicular to \mathbf{b} , the eigenmodes are linearly polarized. It was found in this case that a wave is transmitted if its polarization is collinear to \mathbf{b} and reflected if it is perpendicular to \mathbf{b} ¹⁵. In this configuration, however, Fermi arcs that are present on the surfaces parallel to \mathbf{b} should, in principle, be considered in the analysis.

ACKNOWLEDGMENTS

R. Côté was supported by a grant from the Natural Sciences and Engineering Research Council of Canada (NSERC). R. N. Duchesne and G. D. Duchesne were supported by a scholarship from NSERC and the Fonds de recherche du Québec-Nature et technologies (FRQNT).

Appendix A: CONDUCTIVITY OF A WSM WITH CHERN NUMBER $n = 1, 2, 3$

In this appendix, we show that considering a WSM with a higher Chern number $n = 2, 3$ only multiplies the diagonal elements of the conductivity σ_{xx}, σ_{yy} by the topological charge n when the Hamiltonian is that given by Eq. (1) where the linear dispersion is along the z axis. The conductivity element σ_{zz} gets a more complex dependence²² on n but, as it does not enter in our calculations of the transmission coefficients and Faraday angles, we will not discuss it here.

The current operator is obtained by making the Peierls substitution $\mathbf{k} \rightarrow \mathbf{k} + \frac{e}{\hbar} \mathbf{A}$ in the Hamiltonian and then

taking the derivative $j_\alpha = -\frac{\delta H}{\delta A_\alpha}$, where $\alpha = x, y, z$. In cylindrical coordinates (φ, k_\perp, k_z) , we get for j_x and j_y

$$j_x = -\chi n v_F \beta e \begin{pmatrix} 0 & (k_\perp e^{-i\varphi})^{n-1} \\ (k_\perp e^{i\varphi})^{n-1} & 0 \end{pmatrix}, \quad (\text{A1})$$

$$j_y = -\chi n v_F \beta e i \begin{pmatrix} 0 & -(k_\perp e^{-i\varphi})^{n-1} \\ (k_\perp e^{i\varphi})^{n-1} & 0 \end{pmatrix} \quad (\text{A2})$$

where we have omitted the diamagnetic contributions. In these equations, τ is the node index and n the Chern number. With the eigenvectors given by Eq. (3), the matrix elements of the current operator are for node $\chi =$

+1 and band index $s = \pm 1$

$$\langle \eta_+ (\mathbf{k}) | j^{(x)} | \eta_- (\mathbf{k}) \rangle = -n v_F \beta e k_\perp^{n-1} \times \frac{k_z \cos \varphi + i \sin \varphi \sqrt{k_z^2 + \beta^2 k_\perp^{2n}}}{\sqrt{k_z^2 + \beta^2 k_\perp^{2n}}}, \quad (\text{A3})$$

$$\langle \eta_+ (\mathbf{k}) | j^{(y)} | \eta_- (\mathbf{k}) \rangle = -n v_F \beta e k_\perp^{n-1} \times \frac{k_z \sin \varphi - i \cos \varphi \sqrt{k_z^2 + \beta^2 k_\perp^{2n}}}{\sqrt{k_z^2 + \beta^2 k_\perp^{2n}}}. \quad (\text{A4})$$

For $\chi = -1$, it suffices to make the substitution $|\eta_\pm (\mathbf{k})\rangle \rightarrow |\eta_\mp (\mathbf{k})\rangle$ and multiply the result by -1 . The WSM being isotropic around the z axis, we need, for the current response function, the terms (written here for $\tau = 1$)

$$\int_0^{2\pi} \frac{d\varphi}{2\pi} \langle \eta_+ (\mathbf{k}) | j^{(x)} | \eta_- (\mathbf{k}) \rangle \langle \eta_- (\mathbf{k}) | j^{(x)} | \eta_+ (\mathbf{k}) \rangle = n^2 v_F^2 \beta^2 e^2 \frac{k_\perp^{2n-2}}{k_z^2 + \beta^2 k_\perp^{2n}} \left(k_z^2 + \frac{1}{2} \beta^2 k_\perp^{2n} \right), \quad (\text{A5})$$

$$\int_0^{2\pi} \frac{d\varphi}{2\pi} \langle \eta_+ (\mathbf{k}) | j^{(y)} | \eta_- (\mathbf{k}) \rangle \langle \eta_- (\mathbf{k}) | j^{(y)} | \eta_+ (\mathbf{k}) \rangle = n^2 v_F^2 \beta^2 e^2 \frac{k_\perp^{2n-2}}{k_z^2 + \beta^2 k_\perp^{2n}} \left(k_z^2 + \frac{1}{2} \beta^2 k_\perp^{2n} \right), \quad (\text{A6})$$

$$\int_0^{2\pi} \frac{d\varphi}{2\pi} \langle \eta_+ (\mathbf{k}) | j^{(x)} | \eta_- (\mathbf{k}) \rangle \langle \eta_- (\mathbf{k}) | j^{(y)} | \eta_+ (\mathbf{k}) \rangle = n^2 v_F^2 \beta^2 e^2 k_\perp^{2n-2} \frac{i k_z}{\sqrt{k_z^2 + \beta^2 k_\perp^{2n}}}. \quad (\text{A7})$$

The response function $\chi_{x,x}(\omega)$ for node $\chi = 1$ is

$$\begin{aligned} \chi_{x,x}(\omega) &= -\frac{1}{\hbar} \int_0^{2\pi} \frac{d\varphi}{2\pi} \int_{-k_c}^{+k_c} dk_z \int_0^\infty \frac{dk_\perp}{(2\pi)^2} k_\perp \langle \eta_+ (\mathbf{k}) | j^{(x)} | \eta_- (\mathbf{k}) \rangle \langle \eta_- (\mathbf{k}) | j^{(x)} | \eta_+ (\mathbf{k}) \rangle \\ &\quad \times \left[\frac{\langle n_{-1,\mathbf{k}} \rangle - \langle n_{1,\mathbf{k}} \rangle}{\omega + i\delta + 2E(\mathbf{k})/\hbar} + \frac{\langle n_{1,\mathbf{k}} \rangle - \langle n_{-1,\mathbf{k}} \rangle}{\omega + i\delta - 2E(\mathbf{k})/\hbar} \right] \\ &= -e^2 v_F^2 \frac{1}{\hbar} n^2 \beta^2 \int_{-k_c}^{+k_c} dk_z \int_0^\infty \frac{dk_\perp}{(2\pi)^2} \frac{k_\perp^{2n-1} (k_z^2 + \frac{1}{2} \beta^2 k_\perp^{2n})}{k_z^2 + \beta^2 k_\perp^{2n}} \Theta \left(\hbar v_F \sqrt{k_z^2 + \beta^2 k_\perp^{2n}} - e_{F,1} \right) \\ &\quad \times \left[\frac{1}{\omega + i\delta + 2E(\mathbf{k})/\hbar} - \frac{1}{\omega + i\delta - 2E(\mathbf{k})/\hbar} \right], \end{aligned} \quad (\text{A8})$$

where $\langle n_{s,\mathbf{k}} \rangle$ is the occupation of level \mathbf{k} in band s and the energy is

$$E(\mathbf{k}) = \hbar v_F \sqrt{k_z^2 + \beta^2 k_\perp^{2n}}. \quad (\text{A9})$$

We work at $T = 0$ K and assume that the Fermi level is in band $s = +1$ so that the occupation factors are

$$\begin{aligned} \langle n_{-1,\mathbf{k}} \rangle &= 1, \\ \langle n_{1,\mathbf{k}} \rangle &= \Theta(e_{F,\tau} - E(\mathbf{k})). \end{aligned} \quad (\text{A10})$$

From Eqs. (A5) and (A6), we have $\chi_{x,x}(\omega) = \chi_{y,y}(\omega)$ and since $E(\mathbf{k})$ is even in k_z , Eq. (A7) gives $\chi_{x,y}(\omega) = \chi_{y,x}(\omega) = 0$ when the two nodes are considered as two separate systems (each node is assume to be centered at $k_z = 0$).

If we make the change of variables

$$y = v_F \beta k_\perp^n, \quad (\text{A11})$$

$$x = v_F k_z, \quad (\text{A12})$$

we get for both nodes

$$\begin{aligned} \chi_{x,x}(\omega) &= -\frac{e^2 n}{(2\pi)^2 \hbar v_F} \sum_\chi \int_{-v_F k_c}^{+v_F k_c} dx \int_0^\infty dy \frac{y (x^2 + \frac{1}{2} y^2)}{x^2 + y^2} \Theta \left(\sqrt{x^2 + y^2} - e_{F,\chi}/\hbar \right) \\ &\quad \times \left[\frac{1}{\omega + i\delta + 2\sqrt{x^2 + y^2}} - \frac{1}{\omega + i\delta - 2\sqrt{x^2 + y^2}} \right]. \end{aligned} \quad (\text{A13})$$

As we see, the integrals are independent of the Chern number n which appears only as a multiplicative factor.

If we shift the nodes by $\pm b$ along the k_z axis but still integrate from $-k_c$ to k_c for each node, we get a nonzero result for $\sigma_{xy}(\omega)$ which is given by²⁴ (for $b_0 = 0$)

$$\begin{aligned} \text{Re}[\sigma_{xy}(\omega)] &= \frac{ne^2}{2\pi h} b \\ &+ \frac{ne^2}{16v_F\omega\pi h} (4b^2v_F^2 + 8bv_F^2k_c - \omega^2 + 4v_F^2k_c^2) \ln\left(\frac{2v_Fk_c + 2v_Fb + \omega}{2v_Fk_c + 2v_Fb - \omega}\right) \\ &- \frac{ne^2}{16\omega v_F\pi h} (4b^2v_F^2 - 8bv_F^2k_c - \omega^2 + 4v_F^2k_c^2) \ln\left(\frac{2v_Fk_c - 2v_Fb + \omega}{2v_Fk_c - 2v_Fb - \omega}\right), \end{aligned} \quad (\text{A14})$$

or, to order ω^2 by

$$\text{Re}[\sigma_{xy}(\omega)] = \frac{ne^2b}{\pi h} + \frac{1}{12} \frac{ne^2}{\pi h} \frac{\omega^2 b}{v_F^2 k_c^2 - v_F^2 b^2}, \quad (\text{A15})$$

or for the simplest approximation

$$\text{Re}[\sigma_{xy}(\omega)] = \frac{ne^2b}{\pi h}, \quad (\text{A16})$$

and $\text{Im}[\sigma_{xy}(\omega)] = 0$ for $\omega < 2e_F/\hbar$ which is the frequency range where interesting effects occur in the transmission. With the parameters $v_F = 3 \times 10^5$ m/s, $k_c = 50 \times 10^8$ m⁻¹, we find that the difference between the 3 expressions for $\text{Re}[\sigma_{xy}(\omega)]$ is less than 0.0001 for $b = 1 \times 10^8$ m⁻¹ and 0.001 for $b = 10 \times 10^8$ m⁻¹ in the frequency range $f \in [1, 10] \times 10^{12}$ Hz. We can thus safely use the simplest result given by Eq. (A16) in our calculations.

- ¹ H. B. Nielsen and M. Ninomiya, Phys. Lett. B **105**, 219 (1981).
- ² C. Fang, J. Gilbert, X. Dai, and B. A. Bernevig, Phys. Rev. Lett. **108**, 266802 (2012).
- ³ K.Y. Yang, Y.M. Lu, Y. Ran, Phys. Rev. B **84**, 075129 (2011); G. Xu, H. Weng, Z. Wang, X. Dai, Z. Fang, Phys. Rev. Lett. **107**, 186806 (2011); P. Goswami, S. Tewari, Phys. Rev. B **88**, 245107 (2013); A.A. Burkov, L. Balents, Phys. Rev. Lett. **107**, 127205 (2011); A.A. Zyuzin, S.Wu, A.A. Burkov, Phys. Rev. B **85**, 165110 (2012).
- ⁴ J.H. Zhou, H. Jiang, Q. Niu, J.R. Shi, Chinese Phys. Lett. **30**, 027101 (2013); Y. Chen, S. Wu, A.A. Burkov, Phys. Rev. B **88**, 125105 (2013).
- ⁵ X. Wan, A.M. Turner, A. Vishwanath, S.Y. Savrasov, Phys. Rev. B **83**, 205101 (2011); P. Hosur, Phys. Rev. B **86**, 195102 (2012).
- ⁶ H. Z. Lu, S. B. Zhang and S. Q. Shen, Phys. Rev. B **92**, 045203 (2015); F. Wilczek, Phys. Rev. Lett. **58**, 1799 (1987).
- ⁷ D. T. Son and B. Z. Spivak, Phys. Rev. B **88**, 104412 (2013); S. Das Sarma, E. H. Hwang, Phys. Rev. Lett. **102**, 206412 (2009); M. Lv, S. C. Zhang, Int. J. Mod. Phys. B **27**, 1350177 (2013); J. Hofmann and S. Das Sarma, Phys. Rev. B **91**, 241108(R) (2015).
- ⁸ For a review of Weyl semimetals, see, for example : P. Hosur and X.-L. Qi, C. R. Physique **14**, 857-870 (2013); N. P. Armitage, E. J. Mele, A. Vishwanath, Rev. Mod. Physics **90**, 15001 (2018); A. A. Burkov, Annu. Rev. Condens. Matter Phys. **9**, 359 (2018).
- ⁹ F. Wilczek, Phys. Rev. Lett. **58**, 1799 (1987).
- ¹⁰ L. Wu, M. Salehi, N. Koirala, J. Moon, S. Oh, and N. P. Armitage, Science **354**, 1124 (2016).
- ¹¹ A. A. Zyuzin and A. A. Burkov, Phys. Rev. B **86**, 115133 (2012); Y. Chen, Si Wu, and A. A. Burkov, Phys. Rev. B **88**, 125105 (2013).
- ¹² M. Kargarian, M. Randeria and N. Trivedi, Sci. Rep. **5**, 12683 (2015).
- ¹³ O. Trépanier, R. N. Duchesne, J. J. Boudreault, and R. Côté, Phys. Rev. B **106**, 125104 (2022).
- ¹⁴ Q. Chen, A. R. Jutayiah, I. Oladyskin, M. Tokman, and A. Belyanin, Phys. Rev. B **99**, 075137 (2019).
- ¹⁵ N. M. Chtchelkatchev, O. L. Berman, R. Y. Kezerashvili, Y. E. Lozovik, Physics Letters A **399**, 127296 (2021).
- ¹⁶ J. Wu, Y. Xiang, and X. Dai, Results in Physics **46**, 106290 (2023).
- ¹⁷ C. Yang, B. Zhao, W. Cai, and Z. M. Zhang, Optics Express **30**, 3035 (2022).
- ¹⁸ S. Ghosh, A. Sahoo, and S. Nandy, arXiv:2209.11217v4 [cond-mat.mes-hall].
- ¹⁹ For a recent review, see: C. Guo, V. S. Asadchu, B. Zhao, and S. Fan, eLight **3,2** (2023).
- ²⁰ V. S. Asadchy, C. Guo, B. Zhao, and S. Fan, Adv. Optical Mater. **8**, 2000100 (2020).
- ²¹ A. Gupta 10.48550/ARXIV.2209.07506 (2022).
- ²² See for example, S. Ahn, E. J. Mele, and Hongki Min, Phys. Rev. B **95**, 161112(R) (2017).
- ²³ O. V. Kotov and Y. E. Lozovik, Phys. Rev. B **93**, 235417 (2016).
- ²⁴ K. Sonowal, A. Singh, and A. Agarwal, Phys. Rev. **100**, 085436 (2019).

- ²⁵ P. E. C. Ashby and J. P. Carbotte, Phys. Rev. B **89**, 245121 (2014).
- ²⁶ C. J. Tabert, J. P. Carbotte, and E. J. Nicol, Phys. Rev. B **93**, 085426 (2016).
- ²⁷ S. P. Mukherjee and J. P. Carbotte, Phys. Rev. B **97**, 045150 (2018).
- ²⁸ A. Singh and J. P. Carbotte, Phys. Rev. B **103**, 075114 (2021).
- ²⁹ T. Hayata, Y. Kikuchi, and Y. Tanizaki, Phys. Rev. B **96**, 085112 (2017); Z.-M. Huang, J. Zhou, and S.-Q. Shen, Phys. Rev. B **96**, 085201 (2017).
- ³⁰ M. Born and W. Wolf, *Principles of optics*, (Cambridge University Press, 1980).
- ³¹ J. Zhou, Hao-Ran Chang, D. Xiao, Phys. Rev. B **91**, 035114 (2015).
- ³² G. Krizman, J. Bermejo-Ortiz, M. Goyal, A. C. Lygo, J. Wang, Z. Zhang, B. A. Assaf, S. Stemmer, L. A. de Vaulchier, and Y. Guldner, Phys. Rev. B **106**, 165202 (2022).
- ³³ X. Han, A. Markou, J. Stensberg, Y. Sun, C. Felser, and Liang Wu, Phys. Rev. B **105**, 174406 (2022).
- ³⁴ Y. Okamura, S. Minami, Y. Kato, Y. Fujishiro, Y. Kaneko, J. Ikeda, J. Muramoto, R. Kaneko, K. Ueda, V. Kocsis, N. Kanazawa, Y. Taguchi, T. Koretsune, K. Fujiwara, A. Tsukazaki, R. Arita, Y. Tokura and Y. Takahashi, Nat. Commun. **11**, 4619 (2020).
- ³⁵ M. Kanagaraj, J. Ning, and L. He, Reviews in Physics **8**, 100072 (2022).
- ³⁶ R. Bhandia, B. Cheng, T.L. Brown-Heft, S. Chatterjee, C. J. Palmstrøm, and N. P. Armitage, J. Appl. Phys. **128**, 244303 (2020).
- ³⁷ P. Liu, C. Cui, X.-P. Li, Z.-M. Yu, and Y. Yao, Phys. Rev. B **107**, 085146 (2023).
- ³⁸ S. Yadav, S. Sekh, and I. Mandal, Physica B **656** (2023) 414765.
- ³⁹ S. Das, K. Das, and A. Agarwal, Phys. Rev. B **105**, 235408 (2022).